



A dissimilar welded joint of grade 92 steel and AISI 304L steel obtained using IN82 buttering and IN617 filler: relationship of microstructure and mechanical properties

Hardik Sanjay Surkar¹ · Amit Kumar¹ · Sachin Sirohi² · Shailesh M. Pandey³ · Aleksandra Świerczyńska⁴ · Dariusz Fydrych⁴ · Chandan Pandey¹

Received: 21 December 2023 / Revised: 5 February 2024 / Accepted: 3 March 2024 / Published online: 7 April 2024
© Wrocław University of Science and Technology 2024

Abstract

Unfavourable operating conditions of equipment in the energy industry resulting from high-temperature loads determine the need to use special materials and technological solutions, including welding procedures. In this article, buttering using IN82 (ERNiCr-3) consumables was proposed as a method to improve the weldability of grade 92 steel joined by the gas tungsten arc welding (GTAW) process with AISI 304L (IN617 filler). The microstructural characterization of samples was carried out using an optical microscope, scanning electron microscope (SEM) and energy-dispersive X-ray spectroscopy. The welded joint was further characterized by hardness, tensile (room temperature and at 620 °C temperature) and impact tests. Additionally, the fracture surfaces of tensile and impact tests were studied by SEM. Despite the confirmation of the diffusion of alloying elements and significant changes in their concentration, which indicates the formation of Ti and Nb-rich phases, no welding imperfections were detected and favourable joint structures and acceptable properties were obtained. In particular, this concerns the limitation of the formation of brittle structures and the elimination of the untempered martensitic layer. At the same time, there was a significant decrease in the maximum hardness of heat-affected zone (HAZ) on the grade 92 steel side to a relatively low value of 310 HV, and a minimum tensile strength criterion of 600 MPa was achieved with a simultaneous increase in ductility (35% elongation) of the joint. Comparatively, when compared to a non-buttered welded joint, the joint produced with a buttering layer exhibited an increase in the elongation and impact toughness of the welded joint without any compromise in ultimate tensile strength (S_{ut}). The fracture surface of tensile and impact-tested specimens was also characterized using SEM/EDS. Summarizing all the results, it can be concluded that the proposed GTAW procedure of grade 92 and 304L steels can be used in extreme working conditions, in ultra-supercritical power units or the petrochemical and chemical industries.

Keywords IN82 buttering zone · IN617 weld metal · Tensile properties · Interface characterization · GTAW · Dissimilar welding

✉ Amit Kumar
amitdhananme@gmail.com

✉ Sachin Sirohi
sachinsirohi2008@gmail.com

✉ Dariusz Fydrych
dariusz.fydrych@pg.edu.pl

¹ Mechanical Engineering Department, Indian Institute of Technology Jodhpur, Karwar, Rajasthan 342037, India

² Department of Mechanical Engineering, SRM Institute of Science and Technology, Delhi NCR Campus, Modinagar, Uttar Pradesh 201204, India

³ Mechanical Engineering Department, National Institute of Technology Patna, Patna 800005, Bihar, India

⁴ Institute of Manufacturing and Materials Technology, Faculty of Mechanical Engineering and Ship Technology, Gdańsk University of Technology, Gabriela Narutowicza Street 11/12, 80-233 Gdańsk, Poland

1 Introduction

Dissimilar welded joints (DWJs) of austenitic stainless steels and Cr–Mo grade ferritic steels are unavoidable in ultra-supercritical (USC) power units, petrochemical industries and chemical industries. Austenitic stainless steels are specifically employed in the high-temperature segments of boiler tubing, such as the final stages of the superheaters and re-heaters, where it is crucial to have exceptional resistance to creep rupture and oxidation [1]. On the other hand, low-temperature regions of boiler tubes and heat exchangers are mainly manufactured using the Cr–Mo grade ferritic steels [1–3]. Nevertheless, when it comes to DWJs involving stainless steels and Cr–Mo grade ferritic steels, a substantial variation emerges across the joint concerning chemical composition, microstructure, residual stresses, thermo-physical properties and mechanical properties. Numerous failures of the direct joint of the austenitic stainless steels and Cr–Mo grade ferritic steels have been linked with one or more of the following factors: (1) a significant difference in thermal expansion coefficient (TEC) of austenitic steel ($18.5 \mu\text{m/m/K}$) and ferritic steel ($12.6 \mu\text{m/m/K}$), (2) carbon migration across the interface of the steel and weld metal (WM), and (3) creep strength variation [4–6]. The variation in TEC creates significant residual stresses at the interface between weld and ferritic steel [7]. These high residual stresses can weaken the welded joint over time, potentially leading to its failure or reduced structural integrity [8]. Carbon diffusion typically takes place from the ferritic steel to the austenitic or Ni-based filler welds, leading to the creation of a soft zone at the interface. This soft zone is highly susceptible to deformation and failure, posing a potential weakness in the welded joint [9]. Differences in creep strength between the materials can result in variations in their ability to withstand deformation at elevated temperatures. These differences may, in turn, lead to localized weakening and eventual failure of the joint, particularly when exposed to high-temperature conditions over time [10, 11].

Numerous studies and investigations have been conducted on DWJs with the aim of enhancing their performance and reliability during service conditions [12]. Initially, austenitic fillers were employed for welding these two types of steel. However, the segregation of low melting impurity elements within the welded joint resulted in reduced creep and impact strength, leading to performance issues [13]. Austenitic fillers also produced multiple cracks in the region of the interface. Laboratory test results and actual service conditions have shown that utilizing Ni-based welding consumables provides superior creep and mechanical performance compared to using austenitic fillers [14]. Cao et al. [15] conducted research

on the microstructure and mechanical characteristics of DWJ between T92 martensitic and S304H austenitic steels, which were fabricated using the IN82 filler material. The tensile strength and the impact toughness of dissimilar T92/S304H material joints met the specifications of USC boilers. Notably, the T92 coarse-grained heat-affected zone (CGHAZ) exhibited relatively lower tensile strength, whereas the WM displayed comparatively lower toughness within the joints. Cao et al. [16] assessed the creep resistance of DWJ between T92 martensitic and HR3C austenitic steels, fabricated using the TIG welding process and IN82 filler material. Fracture occurrences were observed within the grade 92 BM when subjected to applied stresses of 140 MPa or higher. However, when the applied stress fell below 140 MPa, the fracture location shifted to the HAZ of the grade 92 BM. Kim et al. [17] evaluated the tensile and creep rupture behaviour of the DWJ of T92 and 304H austenitic steel. The test results showed that failure for both high-temperature tensile and creep tests from T92 BM occurred due to its more rapid degradation with increasing temperature. During creep deformation, the extensive precipitation of Laves phase along the grain boundaries within the FGHAZ was observed. This phenomenon was identified as the primary cause of accelerated void formation in that region, ultimately resulting in premature failure during creep. Extensive research has also been carried out on filler composition and its impact on weld performance. Kumar et al. [18] investigated the influence of varying filler compositions on the high-temperature tensile properties of the DWJ between grade 92 steel and Alloy 617. Based on the investigation of impact and high-temperature tensile properties, the ENiCrFe-3 electrode was selected as the most suitable choice for the SMAW joint between Alloy 617 and grade 92 steel. Based on the research conducted by Hosseini et al. [13], the IN617 filler material was determined to be the optimal choice for achieving the best mechanical properties in dissimilar joints between 310 stainless steel and Inconel 617. Naffakh et al. [19] conducted comprehensive research focussed on optimizing filler materials for dissimilar welding involving AISI 310 and IN657 alloys. The findings indicated that, at room temperature, Inconel A filler material had the best properties than the austenitic filler for DWJ between 310 stainless steel and IN 657. The utilization of the Ni-based filler material significantly improved the performance of the welded joint by effectively addressing carbon diffusion issues. Additionally, it resulted in a reduction of residual stress levels at the interface and enhanced creep resistance under service conditions. Nonetheless, carbon diffusion remains a persistent concern in DWJ, and its subsequent effects continue to impact the mechanical and metallurgical properties of the welded joint [20–22]. Recently, several studies have

been published focussing on minimizing carbon diffusion by incorporating a transition piece between the two metals or by introducing a Ni-alloy buttering layer between them [9, 23–25]. This method aims to combat the formation of both a soft zone and a hard martensitic layer, offering a promising solution to the carbon diffusion problem. Kulkarni et al. [9] employed Incoloy 800 and Inconel 600 interlayers to improve the performance of the DWJ between P91 steel and AISI 316L stainless steel, produced using the A-TIG process. This was achieved by effectively reducing carbon diffusion. The interlayers have also contributed to an improvement in the impact toughness and ductility of the welded joints, all whilst keeping a minimal decrease in tensile strength. Alloy 800 is a preferred choice for use as an insertion piece in DWJ involving ferritic and austenitic steel. It is favoured for its excellent resistance to creep and oxidation, as well as its suitable TEC ($17.1 \mu\text{m}/\text{m}/\text{K}$) positioned between the two metals [4]. Trimetallic transition joints, (ferritic steel-alloy 800-austenitic steel), are currently employed in the piping system of India's Prototype Fast Breeder Reactor (PFBR) [26]. Limited research has been conducted on creating dissimilar joints between high-temperature materials, such as grade 92/AISI 304L, grade 92/AlloyN617 and AISI 304H/IN617, with and without buttering layer [24, 27–33]. Selvi and Reddy [4] investigated the effect of temperature and strain rate on the tensile behaviour of the DWJ of P91 and Alloy 800 produced using the GTAW process with the use of the IN82 buttering layer. Singh et al. [5] also noted an enhanced mechanical and creep performance in the DWJ between AISI 304H and IN617 after the application of an IN617 buttering layer on AISI 304H. The fatigue limit for

the weld with buttering was found to be higher than that of the weld without buttering, with values of 326.8 MPa compared to 306.8 MPa for DWJ of Alloy 617 and 12%Cr steel [33].

Despite previous investigations into dissimilar welds, as mentioned earlier, there is still a need for a comprehensive study aimed at improving the mechanical properties of DWJs of Grade 92 ferritic steel and austenitic AISI 304L steel through the use of a buttering layer. This investigation seeks to evaluate the effectiveness of employing a buttering layer when welding dissimilar materials by comparing their mechanical to those welded without a buttering layer. The study includes a thorough examination of microhardness, tensile strength and Charpy impact toughness. The microstructural analysis supports the observed enhancements in mechanical performance of welded joints made with a modified procedure.

2 Experimental details

2.1 Buttering and welding

Grade 92 steel and austenitic grade AISI 304L steel plates were used in the present work. Electric discharge cutting was used to machine the plate to a three-dimensional size of $120 \text{ mm} \times 55 \text{ mm} \times 8 \text{ mm}$ in order to conduct the experiment. The chemical composition of both steel plates is mentioned in Table 1 [28, 34]. The mechanical properties of both the materials are listed in Table 2. A 2.4 mm diameter IN82 filler (ERNiCr-3) was employed to perform buttering on the grade 92 plate using the gas tungsten arc welding (GTAW)

Table 1 Alloy composition (%wt.) of the grade 92, AISI 304L BMs [28, 34]

| Material | C | Cr | P | S | Si | Ni | Mn | Others |
|-------------------------------------|-------|-------|-------|-------|------|------|------|--|
| Grade 92 steel (9Cr–0.5Mo–1.8W–VNb) | 0.093 | 8.60 | 0.019 | 0.004 | 0.21 | 0.31 | 0.41 | Mo:0.45, Nb:0.052, W:1.98, Ti:0.001, Al:0.001, B:0.002, V:0.18, Zr:0.002, N ₂ :0.060, Fe: Rem |
| AISI 304L | 0.018 | 18.05 | 0.024 | 0.011 | 0.42 | 8.06 | 1.12 | Fe: Rem |

Table 2 Mechanical properties of grade 92 and AISI 304L steel [35–38]

| | Grade 92 BM | AISI 304L | ERNiCr-3 | ERNiCr-CoMo-1 |
|---------------------------------|-------------|-----------|----------|---------------|
| Ultimate tensile strength (MPa) | 758 | 632 | 586 | 690 |
| 0.2% yield strength (MPa) | 520 | 209 | 310 | – |
| % elongation | 33 | 84 | 35 | 45 |
| Micro-hardness (VHN) | 243 ± 2 | 203 ± 3 | 185 ± 7 | – |
| Impact toughness (J) | 185 ± 5 | 285 ± 5 | 135 ± 5 | – |

process. The IN617 filler (ERNiCrCoMo-1) of diameter 2.4 mm was utilised for multi-pass welding using the GTAW process. The chemical composition of both the fillers are mentioned in Table 3. The welded joint was fabricated in the following steps:

Step I: The plate of grade 92 steel and AISI 304L steel of dimension 120 mm × 55 mm × 8 mm were machined from the supplied plate and a conventional V groove configuration was cut at the edges of the plate as per Fig. 1a, b.

Step II: The buttering was performed on the grade 92 plate using the IN82 filler (ERNiCr-3) of diameter 2.4 mm with the GTAW process. The width of the buttering layer was kept between 7 to 8 mm. Four buttering layers were deposited with an average thickness of approximately 2 mm for each layer (Fig. 1c). The welding current and the arc voltage were kept in the range of 100–105 A and 8–9.8 V. The total heat input of buttering was 3.486 kJ/mm.

Step III: The buttered specimen was then subjected to heat treatment at 730 °C for 120 min to relieve the quench stresses and temper the newly formed fresh martensite.

Step IV: After heat treatment, the surface of the buttered grade 92 plate was machined at the edges and cut into a single V groove (Fig. 1d). After the machining, the width of the buttered layer was about 5.8 mm.

Step V: The buttered specimen of the grade 92 plate was welded with an AISI 304L plate as per the configuration mentioned in Fig. 1d. The welding was completed using IN617 filler by GTAW processing in 5 passes. The welding current and arc voltage were kept in the range of 105–116 A and 9.2–10.0 V respectively. The total heat input was 3.162 kJ/mm. The plate after completion of the welding is displayed in Fig. 1e, f.

The welding and buttering procedure took place in an Ar (99.99%) shielding atmosphere, supplied at a flow rate of 10 L per minute. The process was carried out in flat position (PA), the root pass nozzle had a diameter of 6.5 mm, whilst the capping and filling passes used a nozzle with a diameter of 11.5 mm. Both the buttering and welding operations were conducted using the same welding setup, specifically the Fronius Magic Wave 2200. In the GTAW process, a 2.4 mm diameter tungsten electrode (EWTh-2) was employed.

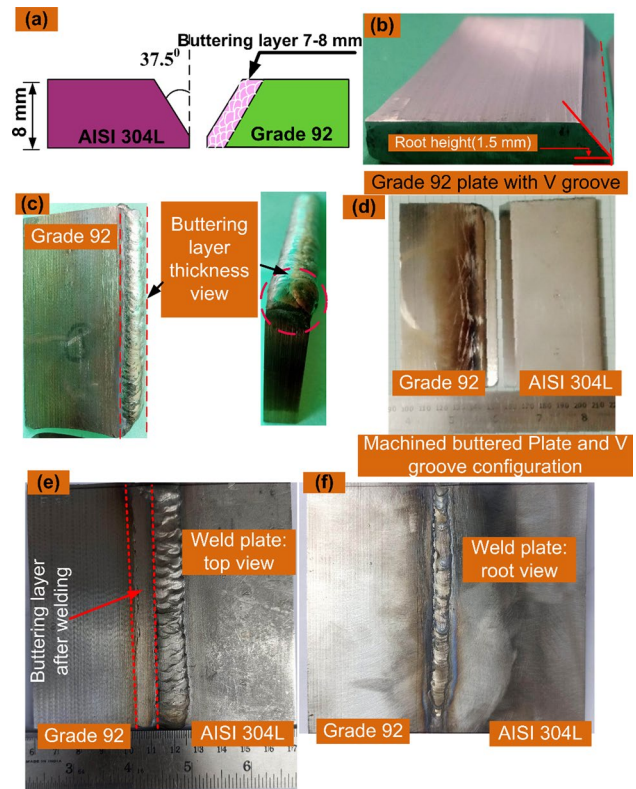


Fig. 1 a V groove configuration with groove details, b machined grade 92 plate with V groove, c plate after deposition of buttering layer of IN82, d position of welding after machining of buttered plate, e, f plate top and root side after welding

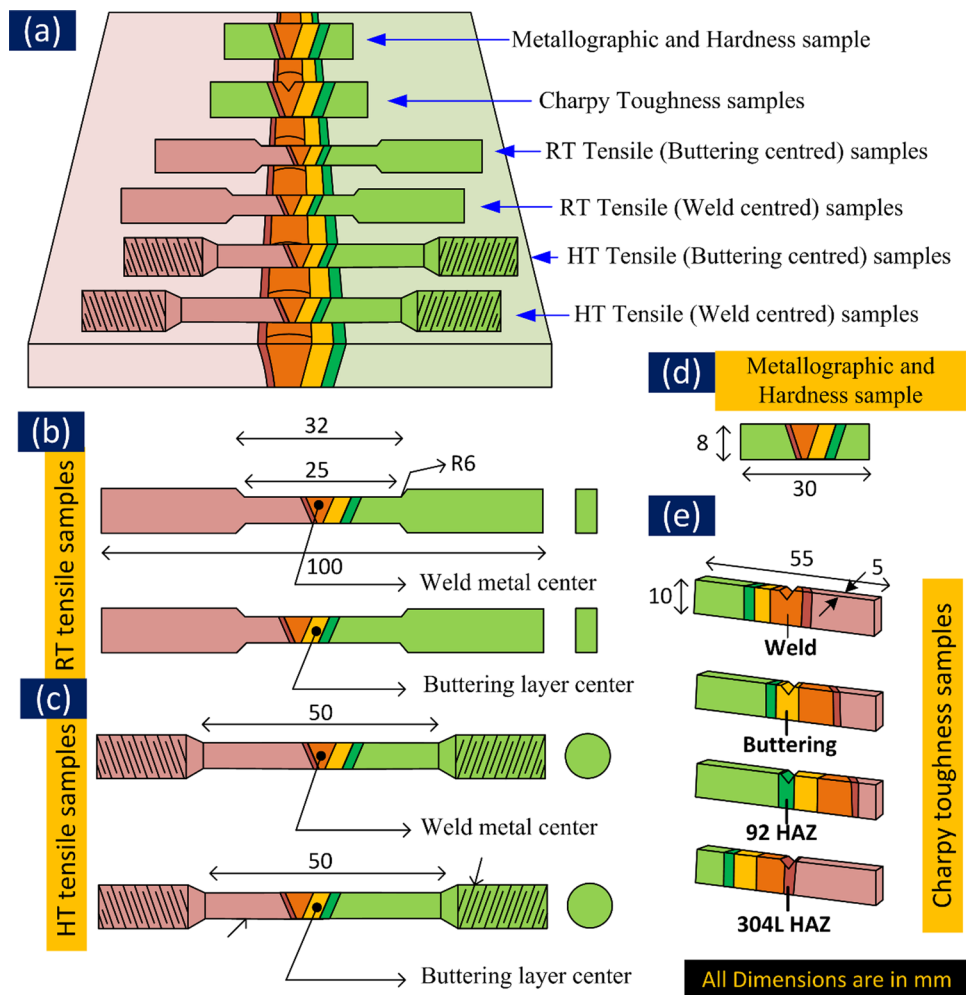
2.2 Mechanical testing and characterization

After fabrication of the welded joint, visual testing and liquid penetrant testing were performed to check the surface defect. There was no defect observed on the welded joint surface. In the next step, samples were extracted from different regions of the welded plate for mechanical and metallography testing (Fig. 2a). A sample of size 30 mm × 8 mm × 8 mm was machined for the metallography study (Fig. 2d). The machined sample was polished using SiC paper of grit size 2000 and then cloth polished in the medium of alumina

Table 3 Chemical composition of IN82 and IN617 filler (wt.%)

| Material | C | Cr | P | S | Si | Ni | Mn | Others |
|--------------|-------|-------|-------|-------|------|-------|------|--|
| ERNiCr-3 | 0.015 | 19.69 | 0.010 | 0.010 | 0.17 | 73.89 | 3.07 | Nb:2.46, Fe:0.13, Ti:0.30, Al:0.08, Cu:0.01 |
| ERNiCrCoMo-1 | 0.08 | 22.00 | .015 | 0.008 | 0.60 | 53.00 | 0.80 | Co:12.00, Mo:9.00, Fe:1.5, Ti:0.20, Al:1.00, Cu:0.20 |

Fig. 2 **a** Schematic of the welded plate and samples extracted for **(b)** room temperature tensile test, **c** high-temperature tensile test, **d** metallographic and hardness characterization **(e)** Charpy toughness test



powder. Samples were then etched with appropriate etchants, mentioned in ASTM E407. For AISI 304L steel, aqua regia ($\text{1HNO}_3 + 3\text{HCl}$) was used as an etchant, whilst for grade 92 steel, Vilella's (1 g picric acid and 5 mL HCl in 100 mL ethanol) was used as an etchant. The weld zone and the buttered zone were electro-etched in oxalic acid 10% at 9 V. The mechanical properties assessment was carried out using tensile, hardness and impact testing. The tensile specimens were machined as per ASTM E8M standards to evaluate the tensile properties of the different zones at room temperature [39] and at high temperature of 620 °C. The poor steam oxidation resistance is the major drawback of grade 92 steel, limiting the operating temperature about 620–630 °C [3, 40]. The specimen with standard dimensions is depicted in Fig. 2b, c. The tensile testing was performed at a constant displacement rate of 1 mm/min. For impact testing, the Charpy specimen of dimension 55 mm \times 10 mm \times 5 mm was machined from the different zones as per ASTM E23 [41]. The samples with notch locations are displayed in Fig. 2e. The hardness measurement across the welded joint was performed at a load of 500 g, as per ASTM E384. The hardness

plot covers the weld zone area, HAZs, buttered zone and base metals.

3 Results and discussion

3.1 Base metals

Figure 3a–d illustrates the microstructures of the base materials AISI 304L steel and grade 92 steel. The microstructure of grade 92 steel illustrated in Fig. 3a, c reveals a tempered martensitic lath structure comprising of prior-austenite grains (PAGs), boundaries (both lath and grain boundaries), as well as coarse and fine precipitates distributed along the lath blocks and grain boundaries. The size of PAGs was measured between 15 and 20 μm [42]. In grade 92 steel, the MX precipitates (ranging in size from 30 to 50 nm) and M_{23}C_6 phases (sized between 100 and 200 nm) are reported as the major precipitates, primarily situated along the boundaries and lath blocks, as depicted in Fig. 3c. Energy-dispersive X-ray Spectroscopy (EDS) analysis of the

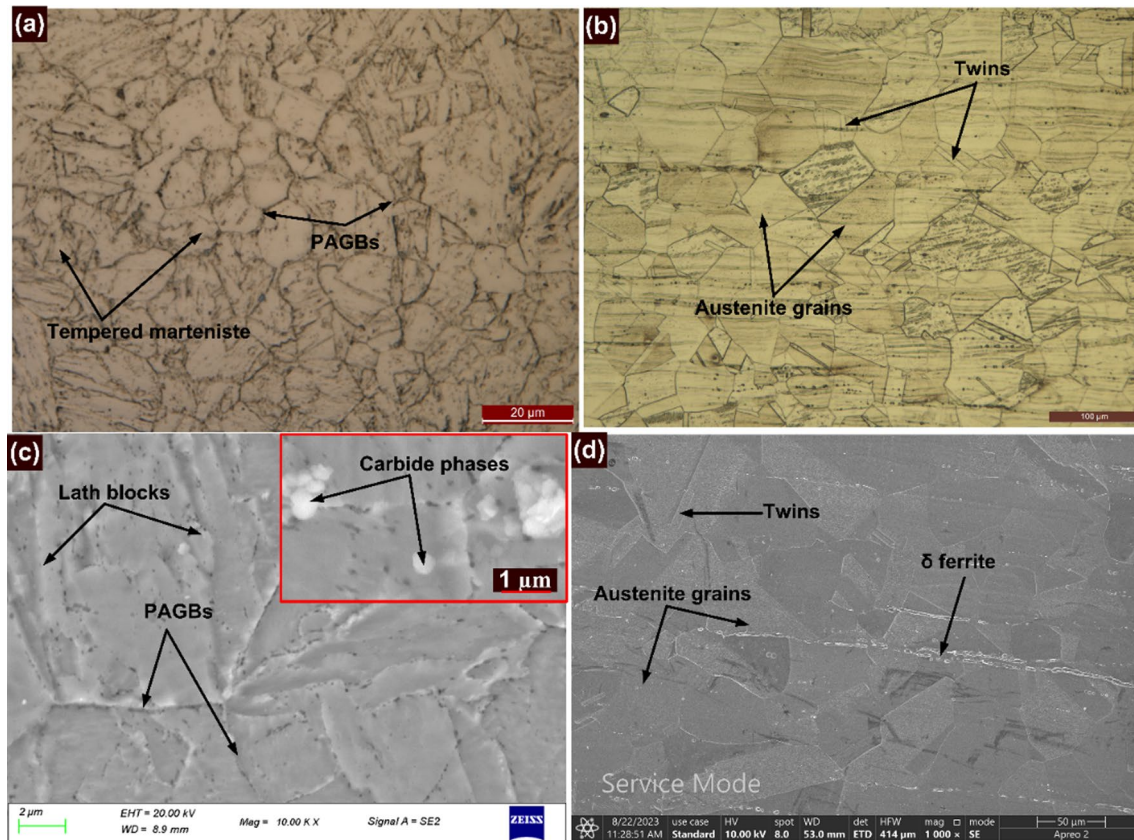


Fig. 3 Optical micrographs of **a** grade 92 steel and **b** AISI 304L steel; SEM images of **c** grade 92 steel and **d** AISI 304L steel

grade 92 steel matrix indicates a major weight percentage of 8.75% Cr, 1.92% W and 84.82% Fe. Furthermore, EDS analysis of coarse white particles (see Fig. 3c) reveals major concentrations of Cr (42.68%), Mo (2.81%) and W (3.45%), implying the possible presence of a phase rich in Cr, Mo and W, which could be the Cr, W and Mo enriched $M_{23}C_6$ phase [43]. A similar observation has also been made in previous study [34]. The microstructure of AISI 304L steel displays the existence of annealing twins and austenite grains (Fig. 3b), with sizes falling within the range of 12–48 μm . Additionally, the presence of δ ferrite is confirmed through examination by both SEM and optical microscopy (Fig. 3b, d). The EDS analysis of the AISI 304L steel matrix indicates significant concentrations of Fe (64.27%), Cr (16.49%), and Ni (8.73%).

3.2 Macrostructure and microstructure of welded joint

Figure 4 shows the macrograph of the welded joints with the buttering zone (BZ). Each zone of the weldments is demarcated, along with its respective width. The width of the weld metal (WM) at the top, the centre and the right regions measured 11.04 mm, 5.97 mm and 2.41 mm, respectively.

The average width of the buttering zone was recorded as 5.80 mm. Notably, the width of the grade 92 HAZ showed variations from the top to the root, ranging between 1.41 mm and 4.96 mm. It's important to mention that the distortion angle remained below 3 degrees for precision. Further characterization of each zone of the weldments was carried out using optical, scanning electron microscopy (SEM), and Energy-Dispersive X-ray Spectroscopy (EDS).

In Fig. 5a, b, the interface region between IN82 BZ and grade 92 BM can be identified. This interface exhibits a sharp region near the fusion line when compared to a non-buttered sample as described in [28]. In the non-buttered sample, the interface was predominantly characterized by macrosegregation features, such as peninsulas, islands and filler-deficient beaches [28]. However, the buttering process has led to the formation of a sharp interface with minimal macrosegregation, likely attributed to improved mixing of BM and buttering filler along the fusion line. Another significant observation at the interface is the elevated concentration of ferrite patches in the grade 92 HAZ adjacent to the fusion line. Previous research has indicated that during buttering, Cr and Ni tend to diffuse from the IN82 BZ into the steel, whilst Fe migrates from the steel into the buttering zone. Laha et al. have observed that an increased

Fig. 4 The macrograph of the weldments produced with ERNiCr-3 (IN82) buttering layer and ERNiCrCoMo-1 (IN617) filler metal

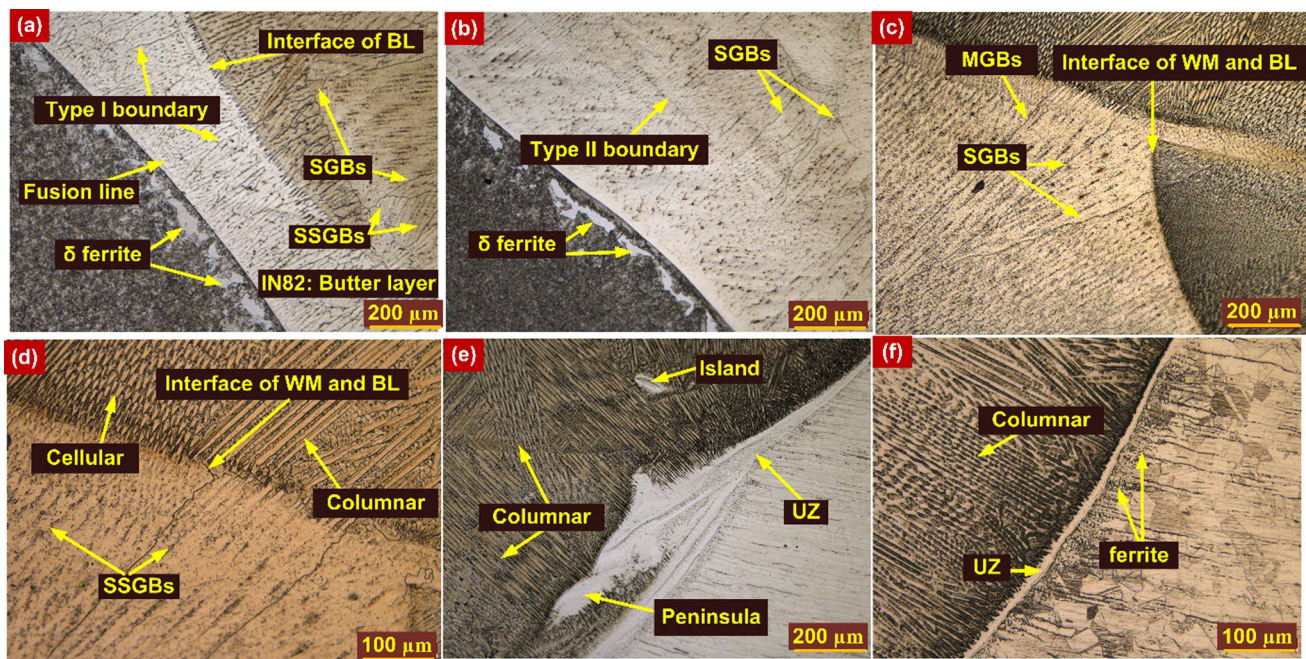
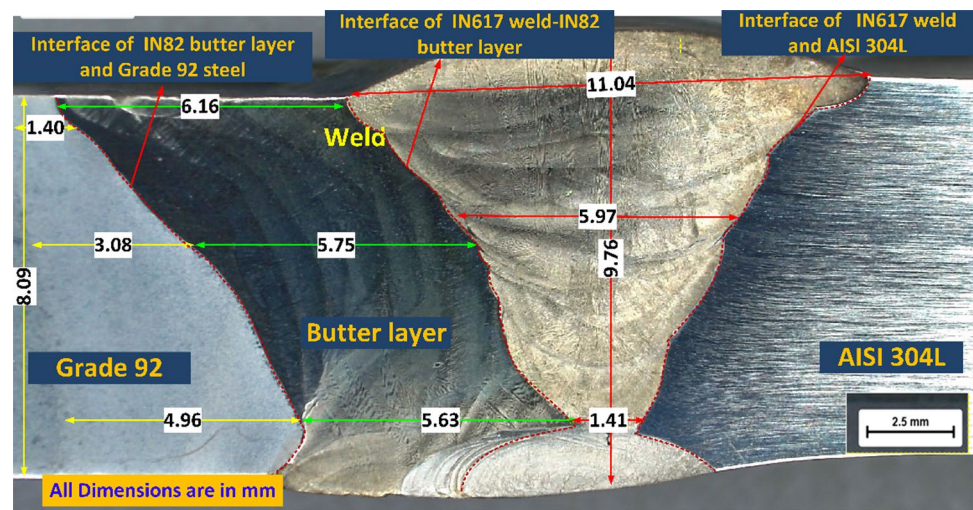


Fig. 5 Optical image of interface of a, b grade 92 BM and IN82 BZ, c, d IN82 BZ and IN 617 WM, e, f IN617 WM and AISI 304L BM

concentration of Ni and Fe at the interface enhances resistance to etching agents [44] which is also seen in Fig. 5a, b. It's worth noting that epitaxial growth does not occur due to significant disparities in chemical composition and crystal structure between grade 92 steel and IN82 BZs. Furthermore, the presence of a Type II boundary [35], consistently aligned parallel to the fusion line, is evident in Fig. 5(b), although it appears discontinuous in some areas of the IN82 BZ, as depicted in Fig. 5a. Additionally, there are Type I boundaries present in the microstructure of the IN82 BZ, resulting from columnar growth originating from the grade 92 BM into the grains (as shown in Fig. 5a) [4]. These Type

I boundaries are oriented nearly perpendicular to the fusion line. Researchers have substantiated that both Type I and Type II boundaries, primarily characterized by high-angle boundaries, are susceptible to stress corrosion cracking (SCC) [4, 45–47]. Surprisingly, discussions regarding their presence in DWJ are rare. A consensus amongst researchers leans towards the idea that Type II boundaries are linked to δ - γ phase transformations occurring in the base metal during welding [45, 46]. In the microstructure of the IN82 BZ (Fig. 5a–c), the solidification grain boundary (SGB), migrated grain boundary (MGB), and solidification subgrain boundary (SSGB) can be identified easily. Notably,

there is an absence of a martensitic layer near the interface, a phenomenon commonly observed in welded joints fabricated without the application of a buttering zone [28]. The formation of a martensitic layer at the interface between the weld and the base metal is typically attributed to changes in chemical composition, carbon diffusion and rapid cooling rates. It's interesting to note that the diffusion of carbon and other alloying elements seems to have no impact on the microstructure and chemical composition of the IN82 BZ. Figure 5c, d displays the interface between the buttering zone of IN82 and the WM of IN617, and both regions are distinguished in the optical image. Despite the similarities in microstructure and melting points between the two fillers, there is a remarkably slender dark region observed at the interface. This phenomenon may be attributed to limited elemental diffusion, which is influenced by variations in chemical compositions. The interface between AISI 304L and IN617 WM is illustrated in Fig. 5e, f. At the interface, there is a filler-deficient zone (FDZ) that manifests as a region with a shortage of filler material, taking on the appearance of beaches (Fig. 5f), islands and peninsulas (Fig. 5e) [48]. The FDZ composition consistently falls within the range intermediate to that of the base metal and the filler metal [49]. The typical AISI 304L HAZ comprises twins, austenitic grains and ferrite, as depicted in Fig. 5f. Notably, the

ferrite density was observed to be higher in the HAZ adjacent to the fusion line, as shown in Fig. 5f.

In dissimilar welding, three distinct fusion line (FL) microstructures were identified: sharp and narrow FL, tempered martensitic microstructure region and wide PMZ [25]. The predominant FL type microstructure, constituting roughly 80–85% of the sharp and narrow FL where the microstructure transitioned from a BCC to an FCC structure without a visibly distinctive transition zone. The ~15% of the FL microstructure consists of the tempered martensitic microstructure region which looks dark and appears less distinct due to the lath-like microstructure. The least common FL microstructure is wide PMZ, which was found only in a few locations and occupied approximately 1–2% of the FL.

Figure 5 demonstrated mainly these three FL types correlated with varying levels of grain coarsening. The major alloying element variations, as determined through SEM/EDS analysis, at the fusion line and interfaces are illustrated in Fig. 6. During the deposition of the buttering layer, the IN82 filler becomes diluted with substrate grade 92 steel which results in the formation of a very narrow partially mixed zone (PMZ) at the fusion interface (Fig. 6a). At other locations, a sharp and narrow FL is seen (Fig. 5a, b). The variation in composition of grade 92 steel and IN82 BZ leads to the composition gradient across the FL which is presented

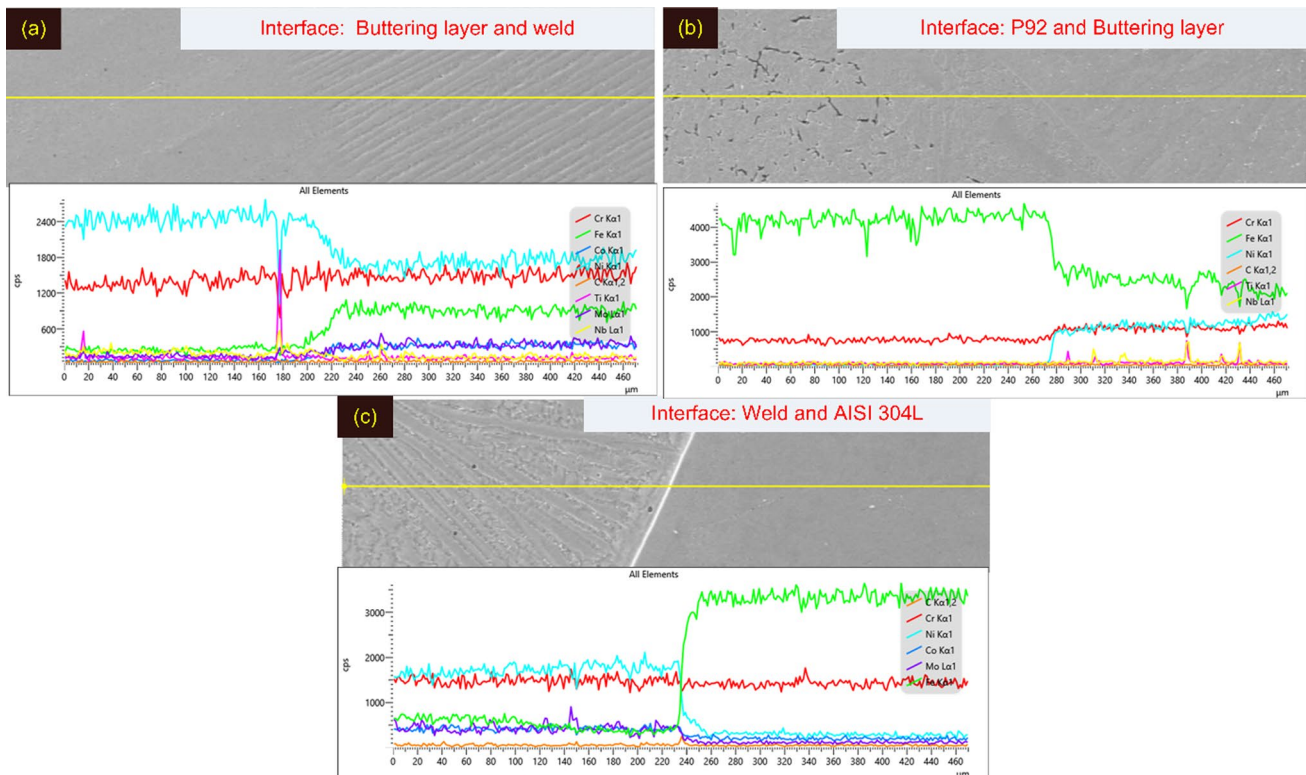


Fig. 6 Alloying element variations by SEM/EDS across **a** interface of grade 92 steel and BZ; **b** interface of BZ and WM, **c** interface of WM and AISI 304L steel

in Fig. 6a. The EDS results, as depicted in Fig. 6a, provide profiles of the primary alloying elements, including Fe, Ni, Nb and Cr. Closer to the FL, there was a noticeable increase in the Fe content, accompanied by a decrease in the Ni and Cr contents. This change in elemental composition resulted in the creation of a dilution zone, extending from the BZ towards the FL. Variations in chemical composition within the PMZ due to dilution can enhance hardenability through the formation of martensite, influenced by the cooling rate during solidification. The significant increase in Ni concentration at the FL markedly raises the probability of austenite phase formation. Furthermore, any elevation in Ni content leads to a lowering of the M_s (martensite start temperature), thereby reducing the likelihood of martensite formation, even when subjected to rapid cooling conditions. The equation is as follows [50]:

$$M_s(^{\circ}\text{C}) = 540 - (497 \times \text{C} + 6.3 \times \text{Mn} + 36.3 \times \text{Ni} + 10.8 \times \text{Cr} + 46.6 \times \text{Mo}) \quad (1)$$

The occurrence of the martensitic zone is frequently observed at the interface between steel and a Ni-based filler weld in the DWJ produced without any buttering layer [23, 24]. This phenomenon may be attributed to the low Ni content at the fusion line, which is required to stop the formation of martensite. The other elements like C, Mn, Cr and Mo also play an active role in the creation of martensite as mentioned in Eq. (1). In the present work, width of the martensitic layer at interface of BZ and grade 92 BM was measured 4–4.5 μm (Fig. 7). The line map across the martensitic layer was captured at higher magnification and presented in Fig. 7. This map reveals a similar pattern to what was depicted in Fig. 6a, showing an increase in the concentration of Fe and a decrease in the concentrations of Ni and Cr as one moves from the BZ to the FL. Notably, an increase in the concentration of C within this layer was also observed (see Fig. 7). The increase in the Nb and Ti peaks within the IN82 BZ (as depicted in Fig. 6a) could be attributed to the presence of phases abundant in Nb and Ti, such as NbC and TiC. Figure 6b shows the EDS map across the interface of the IN82 BZ and the IN617 weld. There is also a composition gradient present at the interface between the BZ and the WM, arising from the differences in the composition of both fillers. However, the change in chemical composition across the interface displays a fully linear profile for Cr and an almost linear profile for Ni and Fe. Additionally, other elements exhibiting changes in concentration are Mo, Co and Nb. As you move from the BZ to the WM, the concentration of Mo and Co increases, whilst the concentration of Nb decreases. At the interface, there is an abrupt increase in the intensity of the Ti peak, which serves as a confirmation of the presence of TiC phases at the interface (Fig. 6b). The

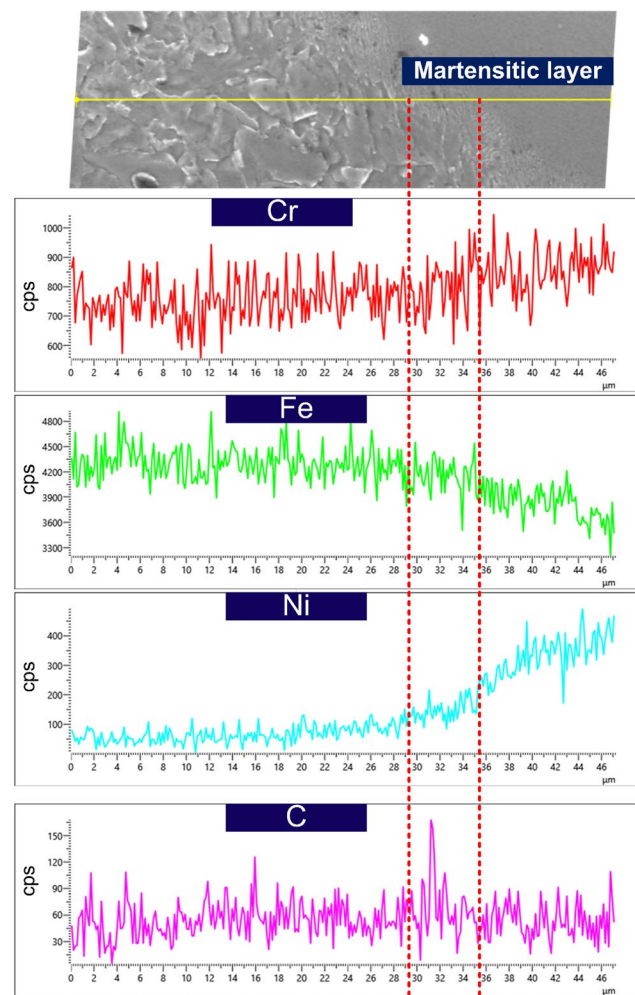


Fig. 7 Line map across the martensitic layer formed at interface of BZ and grade 92 BM

line map across the interface of IN617 WM and AISI 304L BM is displayed in Fig. 6(c). As evident, there is a marked reduction in Ni content along the interface, coupled with an increase in Fe, whereas Cr content exhibits almost negligible change. A sharp decrease in the concentration of the Mo and Co is also observed as moves from WM to AISI 304L BM.

Figure 8 shows the microstructure of the IN82 BZ and IN617 WM. The distinctive development of columnar austenite grains, oriented perpendicular to the FL and aligned with the heat transfer direction, is readily observable in IN82 BZ. A similar type of growth is also confirmed from the previous work of Hytönen et al. [25] and Priya et al. [5]. Figure 8a–c displays the presence of SGBs, SSSBs and MGBs [34]. IN82 BZ near interface also confirms the presence of the crack susceptible type II grain boundary (Fig. 8a). The formation of these boundaries can be attributed to grain growth that occurred during the buttering process. The interface of two layers of buttering is visible in Fig. 8b. The grain size in the BZ is noticeably larger when

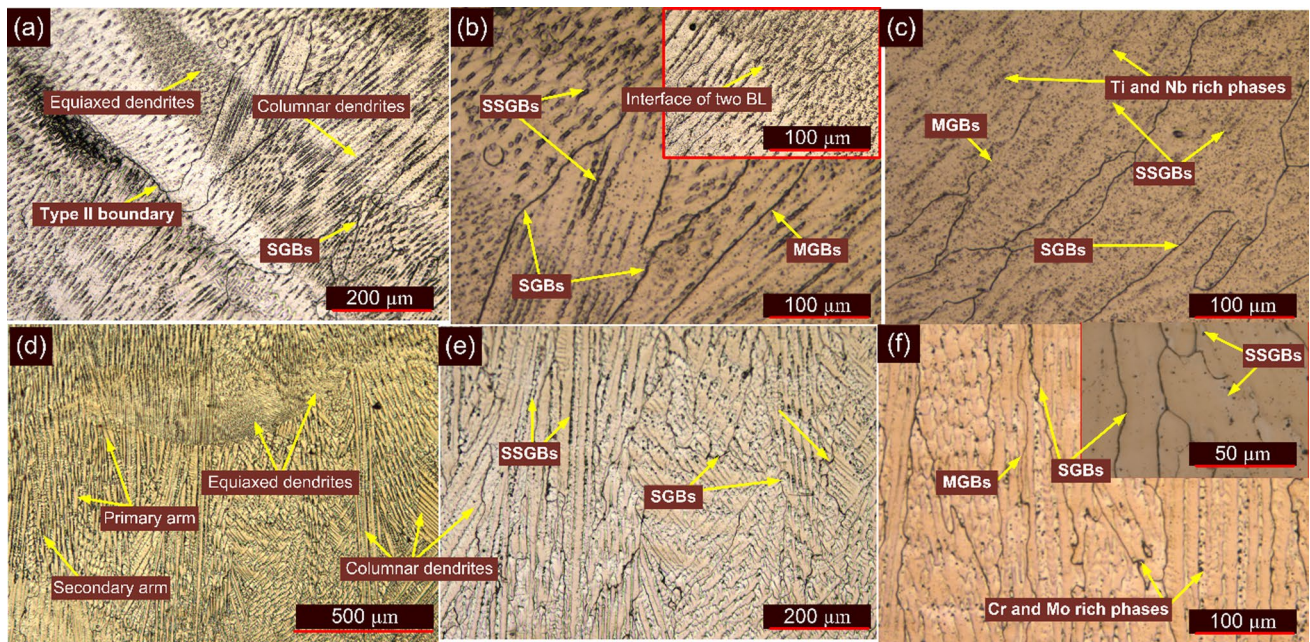


Fig. 8 BZ captured at different locations with different magnifications: **a** showing growth of dendrites near fusion line, **b** interface of two layers of buttering (BL), **c** centre of buttering zone demonstrat-

ing various types of boundaries, including SSGBs, SGBs and MGBs; **d–f** IN617 WM captured at different magnification showing dendritic structure and boundaries

compared to the WM. An image of the IN82 BZ captured at $200\times$ magnification reveals the presence of boundaries and the segregation of alloying elements along them (Fig. 8c). The segregation of alloying elements in IN82 base metal (BZ) primarily results in the formation of secondary phase particles within the microstructure. These secondary phase particles are reported to be complex Ti/Nb carbides.

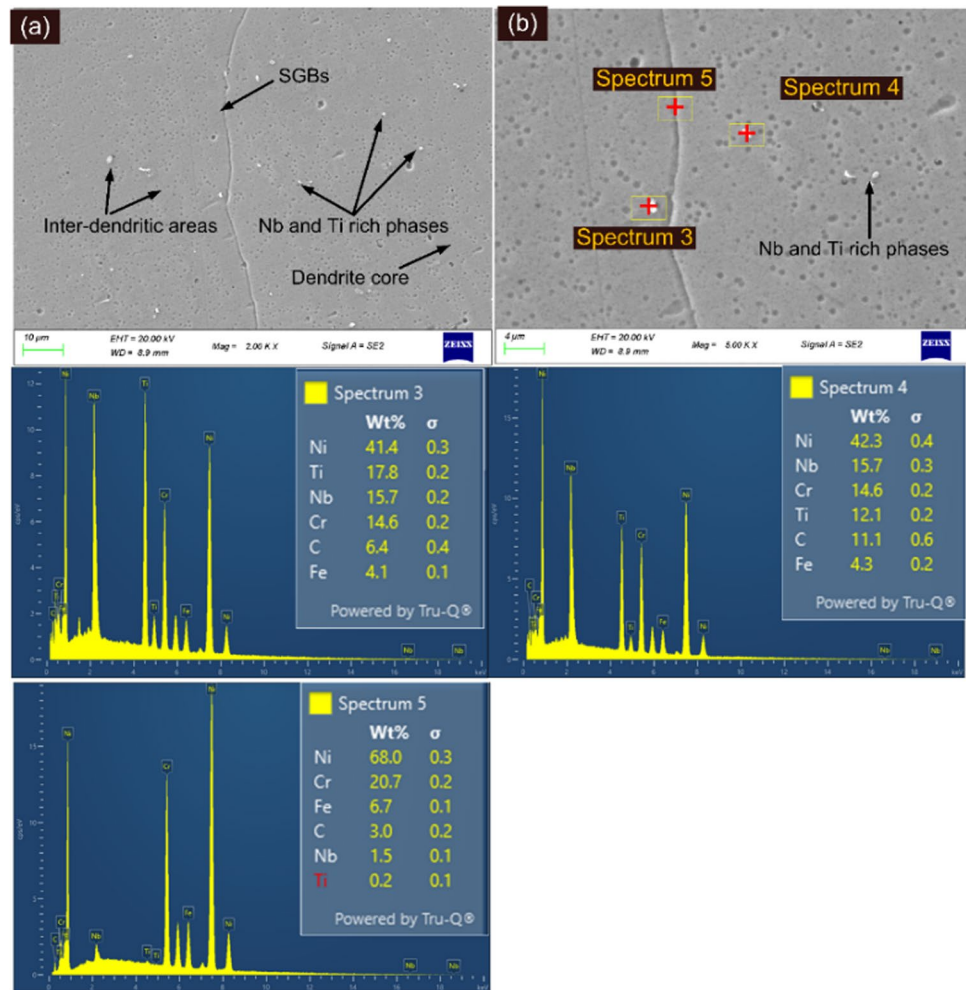
The segregation of alloying elements in the IN82 BZ primarily results in the formation of secondary phases within the microstructure, which are reportedly complex Ti and Nb carbides [32]. Figure 9 shows SEM/EDS analyses of secondary phases found within the microstructure of the IN82 buttering layer. The SEM image represents the boundaries and dispersion of the secondary phase particles along SGBs and inter-dendritic areas (Fig. 9a). In Fig. 9b, the particles and specific points along the SGBs have been marked for the EDS analysis. The EDS of cubic diamond-shaped particles (spectrum 3 and spectrum 4) provide confirmation that these particles are enriched with Ti (12.1–17.8 wt.%) and Nb (15.7 wt.%), suggesting that they are TiC/NbC carbides [34]. The EDS analysis conducted at the SGBs reveals a significant weight percentage of Cr, accounting for approximately 20.7 wt.%. This high concentration of Cr can potentially lead to the formation of the $M_{23}C_6$ phase under certain conditions. The weight % of Nb at SGBs was 1.5%. Interestingly, considering the low C content in the IN82 buttering layer, the presence of these TiC/NbC carbides implies that C has diffused from the grade 92 BM towards the BZ. This

C diffusion not only leads to the formation of TiC/NbC carbides but also has the potential to give rise to other carbides rich in Cr/Mo.

The IN617 WM primarily exhibits a dendritic microstructure, featuring both columnar and equiaxed dendrites, as indicated in Fig. 8d. The detailed view is presented in Fig. 8e, f. The dendrite core and the dendritic arm (primary and secondary arm) are observed clearly from Fig. 7e, f. The boundaries, including SGBs and SSGBs, have been highlighted in Fig. 8d–f. In comparison to the IN82 BZ, the IN617 WM exhibits a significantly lower number of MGBs and it might be due to the higher density of alloying elements in IN617 WM. The spaces between the dendrites, which contain the alloying elements, are depicted in Fig. 8f. The phase morphology and their segregation along the inter-dendritic spaces are displayed in the SEM image (Fig. 10a, b). The greater concentration of secondary phases in the IN617 weld, as compared to the IN82 BZ, is further substantiated by observations in both Figs. 9 and 10.

Figure 10a displays the dendritic structure of IN617, featuring a dendrite core surrounded by inter-dendritic regions exhibiting the segregation of alloying elements Cr and Mo. The region selected for the EDS study is marked in Fig. 10b. The inter-dendritic region's precipitates are confirmed to have an enrichment in Mo and Cr by the EDS examination (spectrum 6: 24.4 wt.% Cr and 17.7 wt.% Mo; spectrum 7: 26.4 wt.% Cr and 26.0 wt.% Mo). Furthermore, it is possible that these precipitates

Fig. 9 **a** IN82 BZ showing core, boundaries and tiny phases dispersed along boundaries and matrix, **b** showing boundaries and precipitates marked for EDS analysis confirming the phases TiC and NbC (spectrum 3 and 4) and Cr, Fe and Ni presence at boundaries (spectrum 5)



are composed of the Cr and Mo-rich phases $M_{23}C_6$ and M_6C . By successfully pinning the grain boundaries, the $M_{23}C_6$ phase of the IN617 weld contributes significantly to high-temperature strengthening [27]. The presence of large Mo-rich M_6C carbides and fine Cr-rich $M_{23}C_6$ carbides specifically located at the inter-dendritic regions of IN617 weld has also been reported in previous research [27]. These findings are further supported by the results of the EDS line scan (see Fig. 6c), captured along the interface of IN617 WM and IN82 BZ. The dendrite core shows notable enrichment in Fe, Co and Ni, as indicated by the data from Spectrum 8. The presence of the Ti(C, N) phase has also been previously documented in other research related to IN617 filler welds [37]. Zhnag et al. [51] also observed the presence of Ti-rich precipitates with diameters ranging from 2 to 3 μm in IN617 filler weld. In the EDS analysis, the presence of a new phase known as the titaniferous phase has been confirmed by Zhnag et al. [51]. This phase is known to form during welding processes conducted at temperatures exceeding 973 K. The presence of these carbides is likely to contribute to an increase in

the microhardness of IN617 weld whilst simultaneously leading to a decrease in impact toughness.

3.3 Mechanical properties of the welded joint

Figure 11 illustrates a hardness profile across the transverse direction of the welded joints. The hardness ranges from a minimum of 198 HV in the base metal of AISI 304L to a maximum of 334 HV in the FGHZ of grade 92. The average hardness for grade 92 and AISI 304L BMs was 239 ± 2 HV and 202 ± 2 HV, respectively. The hardness of the IN82 BZ measured at 221 ± 8 HV was found to be lower than the IN617 WM, which exhibited a hardness of 276 ± 6 HV. For similar IN82 buttering layer, the hardness of the BZ was reported 219 ± 15 HV in previous study of Dak et al. [34]. Despite both the BZ and WM displaying an austenitic microstructure, as shown in Fig. 12, their significant difference in hardness may be attributed to variations in alloying elements and their precipitation behaviour. In the IN82 BZ, the predominant precipitates were NbC and TiC, as observed in Fig. 9. In contrast, the IN617 WM exhibited the presence

Fig. 10 **a** IN617 WM showing core, boundaries and carbide phases dispersed along inter-dendritic spaces, **b** showing boundaries and precipitates marked for EDS analysis confirming the phases Mo-rich M_6C carbides and fine Cr-rich $M_{23}C_6$ carbides (spectrum 6 and 7) and Ni, Fe and Co presence at dendrite core (spectrum 8)

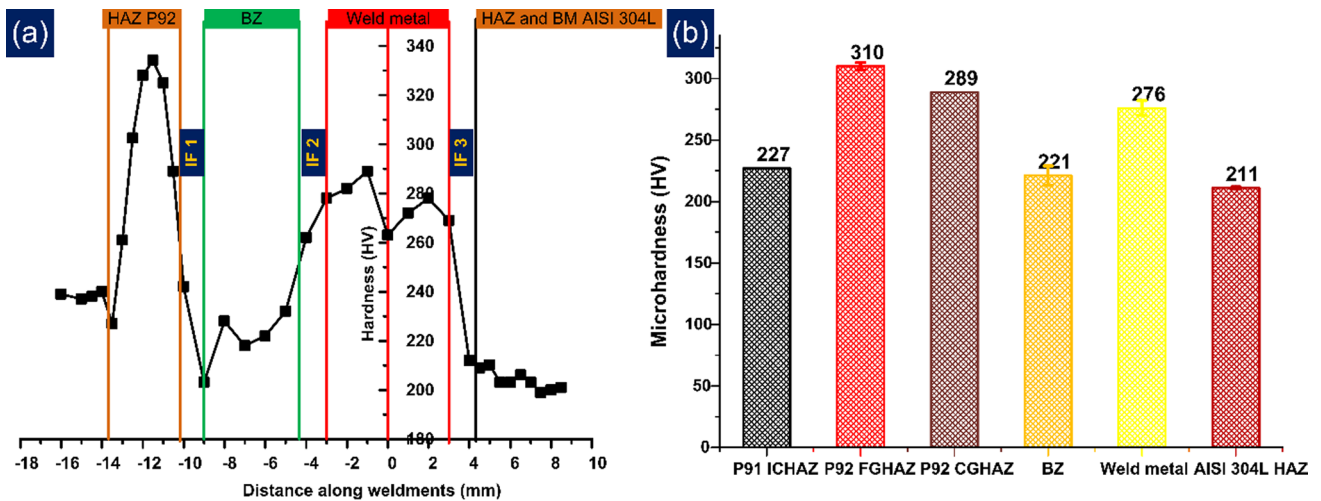
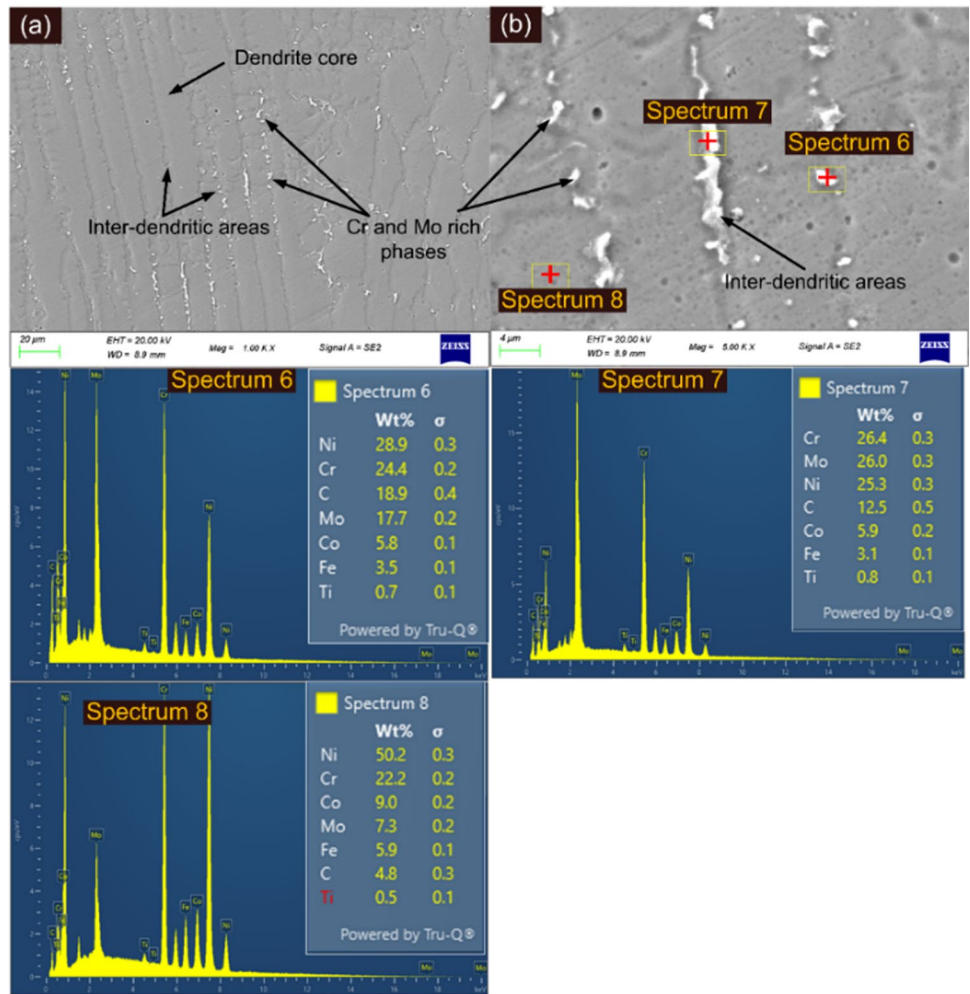


Fig. 11 **a** Hardness plot along the weldments, **b** Various zone of weldments and their corresponding hardness values

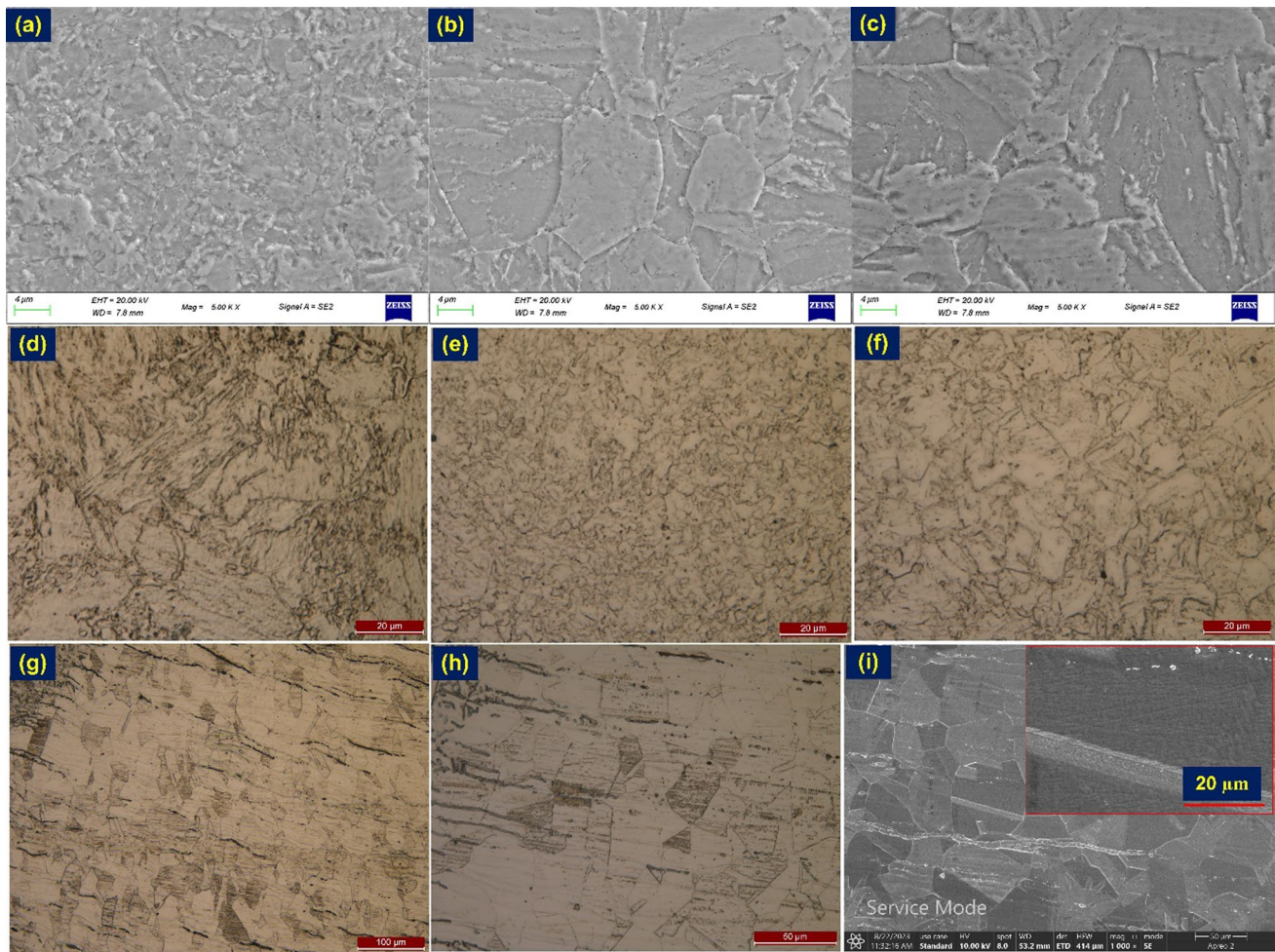


Fig. 12 HAZs formed along grade 92 side: **a, d** CGHAZ, **b, e** FGHAZ, **c, f** ICHAZ, **g–i** HAZ formed along AISI 304L steel side

of $M_{23}C_6$ and Mo_6C precipitates, as shown in Fig. 10. The higher hardness observed in the IN617 WM can also be attributed to the solid solution strengthening provided by the presence of Mo and Co in the IN617 filler material. The decreased hardness observed in the IN82 BZ compared to the IN617 WM can also be attributed to a slightly lower carbon content in the IN82 BZ. In the IN82 BZ, the hardness varies between 203 and 232 HV, whilst in the IN617 WM, it ranges from 263 to 289 HV. The variations in hardness observed in both the IN82 BZ and IN617 WM can likely be attributed to the cumulative heating effects of multi-pass deposition during welding/buttering. Additionally, variations in chemical composition within the microstructure, often resulting from the segregation of alloying elements, may also contribute to these differences in hardness. In a similar joint created using IN617 filler without the buttering layer, the hardness was measured at 254 HV, which is lower than the current hardness value of 276 ± 6 HV [52]. However, for the joint produced without the buttering layer, using IN82 filler, the hardness was measured at 185 HV,

which is significantly lower than the current hardness value of 276 ± 6 HV for the joint with the buttering layer [28]. The hardness at the interface between the IN617 WM and the IN82 BZ (IF2) measured at 262 HV falls between the average hardness values observed for the IN82 BZ and the IN617 WM. This phenomenon is likely a result of elemental variations and the diffusion of elements at the interface, as observed in Fig. 6b. In the non-buttered sample, the hardness distribution reveals spikes on the grade 92 side, with a peak hardness reaching 445 HV in the CGHAZ [28]. This increase in hardness was attributed to the formation of untempered martensite. The presence of the buttering layer effectively eliminates the hardness spikes near the interface on the grade 92 side, as given in Fig. 11a. After applying the buttering layer, the hardness in the grade 92 CGHAZ was measured at 289 HV (Fig. 11b), indicating a reduction of 156 HV compared to the previous hardness level. This reduction in hardness occurred due to the elimination of the untempered martensitic layer. The multi-pass buttering layer deposition introduced tempering reactions, which led

to a decrease in dislocation density and the tempering of the martensite in the grade 92 CGHAZ. Figure 12a, d also confirms the presence of the partially tempered martensite in grade 92 CGHAZ. The hardness of the grade 92 FGHAZ in the non-buttered sample was measured at 362 HV [28], which is nearly similar to the current hardness value of 310 \pm 4 HV. The hardness of FGHAZ is attributed to the presence of untempered martensite with partially dissolved carbide precipitates. The optical and SEM image of FGHAZ is displayed in Fig. 12b, e. In both the non-buttered and buttered welded joints, the lower hardness in the grade 92 HAZs was measured in the ICHAZ with values of 217 HV [28] and 227 HV, respectively. The poor hardness could be due to the formation of soft ferrite (austenite transform product) and the coarsening of the carbide particles [53]. The micrographs of the grade 92 ICHAZ showed the presence of over-tempered martensite (Fig. 12f) and coarse carbide precipitates (Fig. 12c). The hardness of the interface of IN82 BZ and grade 92 BM (IF1) was 242 HV which was lower than the IN82 BZ and close to grade 92 BM (239 \pm 2 HV). The hardness of the AISI 304L HAZ was 211 \pm 2 HV which was close to the hardness of AISI 304L BM (202 \pm 2 HV). The slight increase in hardness of AISI 304L HAZ compared to BM might be attributed to the higher density of ferrite in the AISI 304L HAZ, as observed in the microstructure (Fig. 12g–i). At interface of AISI 304L steel and IN617 weld metal (IF3), hardness was recorded 212 HV. The SEM image of the AISI 304L HAZ also reveals the presence of carbide particles located near the twin boundaries (Fig. 8i).

The impact test outcomes for the welded joints are illustrated in Fig. 13. The test specimen before and after fracture is illustrated in Fig. 13a. The impact toughness of the BZ was determined to be approximately 72 \pm 4 J, whilst the WM exhibited an impact toughness of approximately 103 \pm 5 J. The WM was formed using the IN617 filler, and it was expected to exhibit inferior impact toughness compared to the BZ, which was formed using the IN82 filler. This expectation was based on the higher alloying elements present in the IN617 filler, which are known to have a greater tendency for segregation. The grade 92 HAZ exhibits an untempered martensitic microstructure, as shown in Fig. 12a, and this microstructure results in a lower impact toughness of approximately 84 \pm 4 J. The AISI 304L HAZ exhibited the impact toughness of 132 \pm 2 J. The specimen of grade 92 HAZ and BZ showed the complete fracture into two halves during the impact testing. The specimen failed after impact testing was characterized using the FESEM and displayed in Fig. 13b–e. The fractured surface of weld specimen revealed the major presence of brittle area and shallow dimples in few regions (Fig. 13b). Additionally, EDS analysis (E1) confirmed the presence of secondary phases characterized by high Cr and Mo content. In the fractured specimen of BZ, a significant portion was found to comprise brittle areas, as

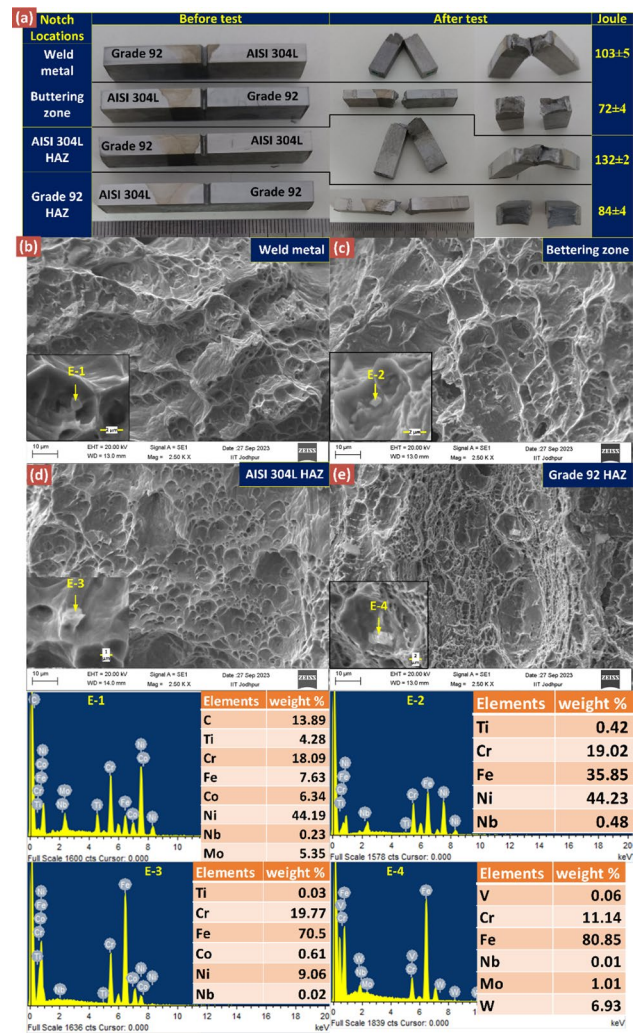


Fig. 13 a Specimen before and after fracture; SEM image of impact fractured surface along with EDS b WM, c buttering zone, d AISI 304L HAZ, e grade 92 HAZ

depicted in Fig. 13c. The extent of brittle areas observed in the BZ was greater than that in the WM. The EDS analysis revealed a predominant concentration of Ni and Fe (E2), with the elevated weight percentage of Fe potentially attributed to the propagation of cracks from the BZ to the grade 92 HAZ. The fractured specimen of AISI 304L HAZ exhibits a distinctive pattern of shear dimples alongside brittle areas. Notably, the dimple density in the HAZ is observed to be greater than that in both the WM and the BZ (Fig. 13d). The EDS analysis of the particle observed at the fracture surface indicated a significant concentration Ni and Cr (E3). This suggests that the particle may be the Cr-rich $M_{23}C_6$ phase. The sample tested in the grade 92 HAZ exhibited a ductile fracture mode, characterized by a higher density of fine dimples with only a few brittle regions present (Fig. 13e). However appearance of the fracture surface does not support the impact test results. The secondary phases observed on

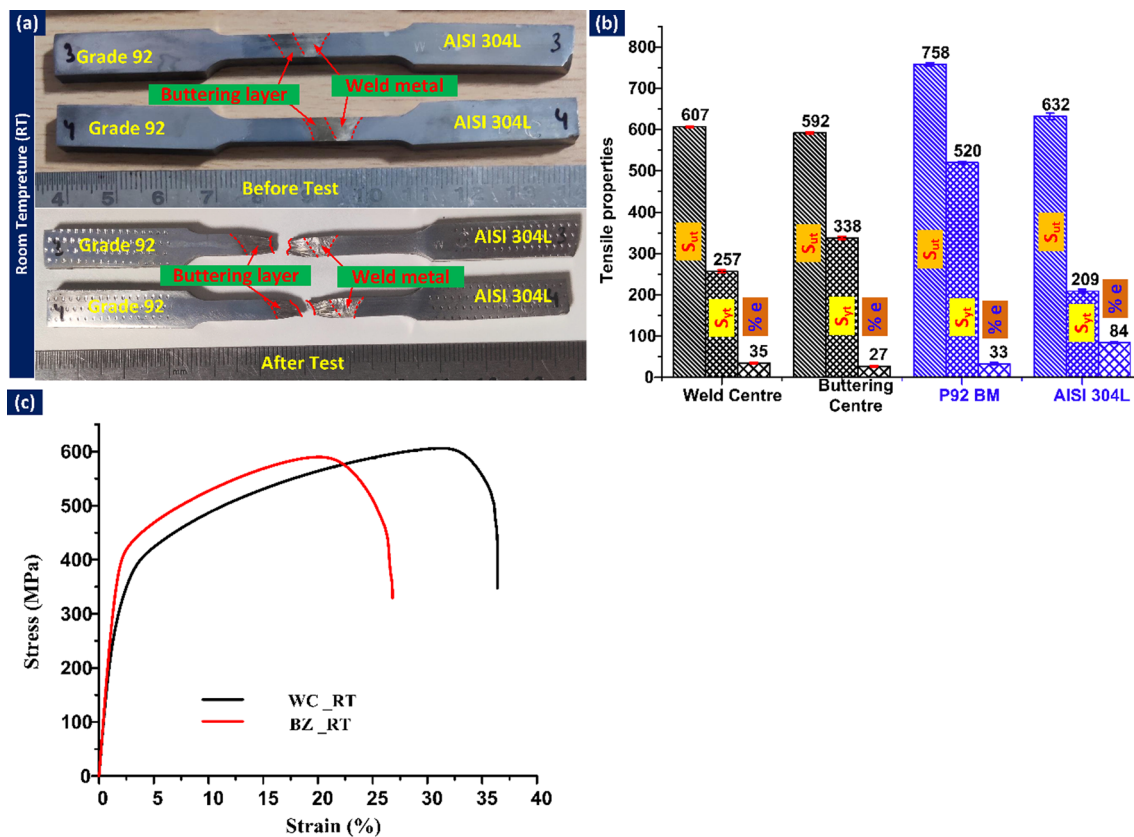


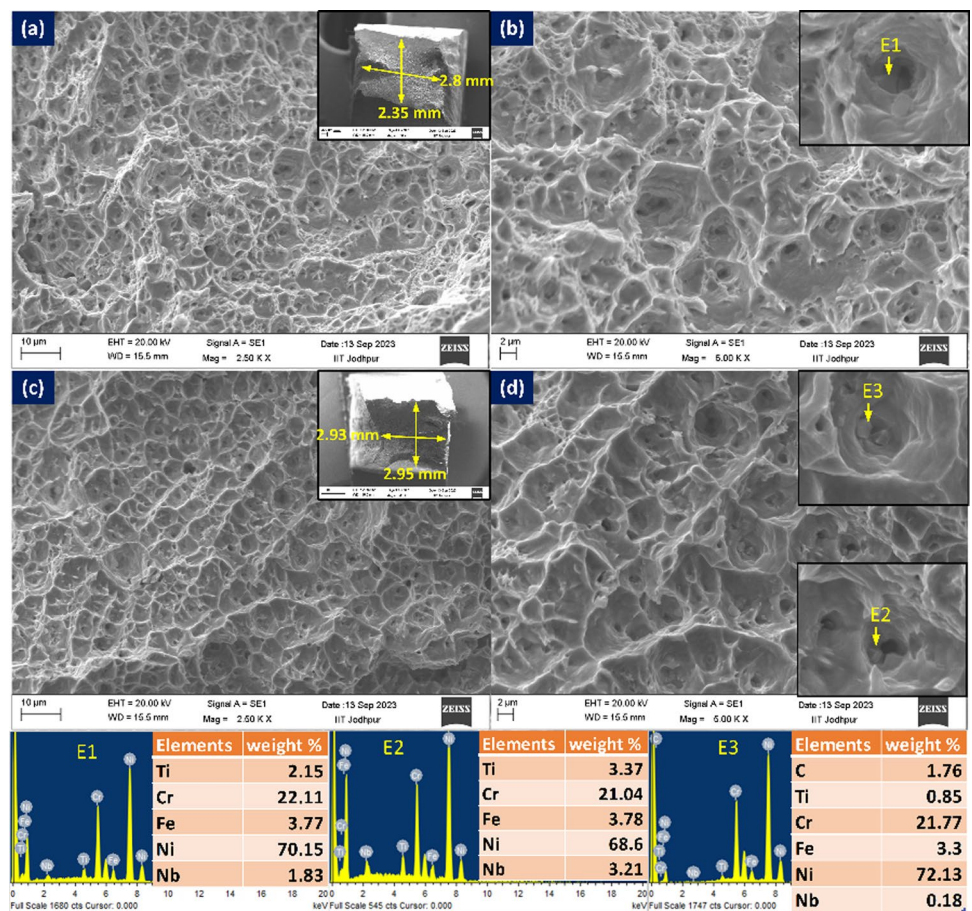
Fig. 14 **a** Specimen before and after fracture, **b** variation in tensile properties of welded joint including base metals [35–37], **c** stress–strain plot of welded joint

the fracture surface have been confirmed as carbides rich in Cr, W and Mo of the $M_{23}C_6$ type (E4).

Figure 14a illustrates the macrograph of the specimens both before and after fracturing. The specimens used for testing the WM are referred to as WC_RT, whilst the one for the buttering zone is denoted as BZ_RT. The test results are presented in Fig. 14b, which also includes the properties of the base metals. Additionally, Fig. 14c provides the stress–strain plot for the welded specimen. The test results revealed specimen failure originating from the buttering zone (BZ) (Fig. 14a) for both WC_RT and BZ_RT, with an ultimate tensile strength (S_{ut}) of 607 ± 2 MPa and 592 ± 2 MPa, respectively. The S_{ut} of WC_RT and BZ_RT was found to be lower than that of the base metals (AISI 304L: 632 ± 6 MPa and grade 92: 758 ± 4 MPa) (Fig. 14b). In a prior study conducted by Dak et al. [28], they reported that the S_{ut} of a welded joint with a similar grade 92/AISI 304L joint, produced using the IN82 filler without a buttering layer, was 610 MPa. However, the fracture location was identified within the IN82 WM. In a separate study involving a similar joint configuration with IN82 buttering and IN82 WM, the S_{ut} for WC_RT was measured at 612 MPa, which closely aligns with the current S_{ut} value. However, for

similar joints, the S_{ut} of BZ_RT was reported as 628 MPa, which was higher than the S_{ut} observed in the current study. The reason for failure from the IN82 BZ instead of the IN617 WM could be attributed to the higher hardness of the IN617 WM compared to the IN82 WM, as indicated by the hardness plot. The minimum S_{ut} requirement for the IN82 filler has been reported at 600 MPa in one study [32], whilst in another research work, it was reported as 586 MPa [35]. Therefore, the welded joint obtained with the IN82 buttering layer meets the minimum S_{ut} criteria required for USC boiler applications, as it exceeds the reported minimum S_{ut} values of 600 MPa and 586 MPa for the IN82 filler from different research sources. Another noteworthy observation following the application of the buttering layer was the shift in the fracture location, accompanied by a substantial increase in the % elongation. Previously, it was situated within the IN82 WM with a % elongation of 19% [28], but in this study, the fracture point shifted to the IN82 BZ with a % elongation of $35 \pm 2\%$. The deformation in BZ is also confirmed by the macrograph displayed in Fig. 14a. The test specimen BZ_RT exhibits a decrease in S_{ut} of 15 MPa and a decrease in % elongation of 8% when compared to WC_RT. The yield strength (S_{yt}) was measured at 257 ± 4 MPa for

Fig. 15 Fracture surface revealing the dimples and voids in FESEM image for (a, b) WC_RT, (c, d) BC_RT along with EDS of the particles present at the fracture surface

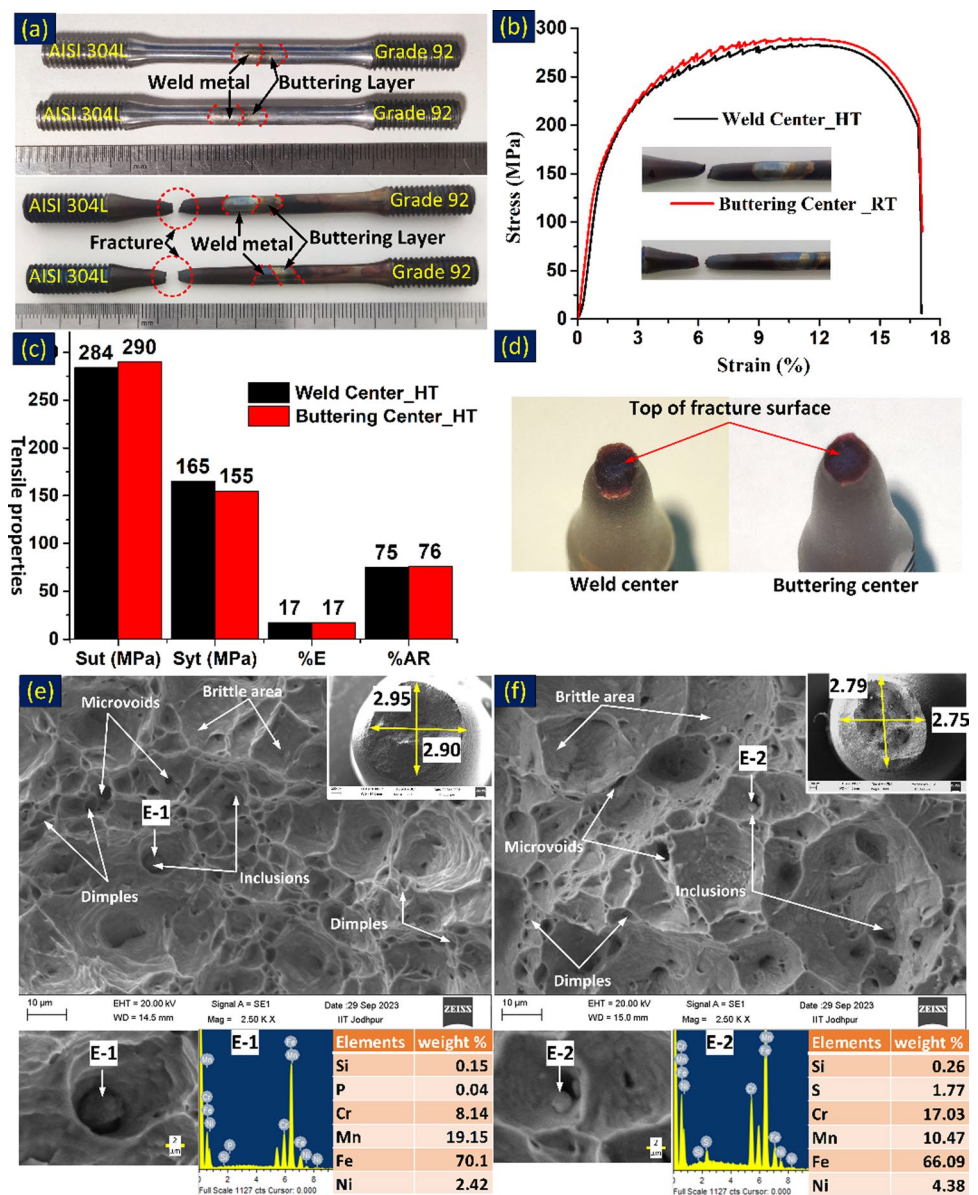


WC_RT and 338 ± 4 MPa for BZ_RT, respectively. These values were higher than the S_{yt} of the AISI 304L BM but lower than that of the grade 92 BM, as shown in Fig. 14b. The fractured specimen underwent a FESEM study, and the resulting image is presented in Fig. 15. The fractography analysis of both WC_RT and BC_RT samples indicates a mixed mode of failure, characterized by a combination of brittle features (cleavage area) and ductile features (dimples and voids). However, dimples and voids are the predominant features on the fracture surfaces of both WC_RT (Fig. 15a, b) and BC_RT (Fig. 15c, d). Notably, the fracture surface of BC_RT exhibits a lower density of shallow dimples compared to WC_RT. A higher density of dimples is indicative of a ductile-dominated fracture mechanism. In both samples, the failure occurred in the buttering layer, which is confirmed by the EDS results (EDS 1, EDS 2 and EDS 3) revealing the presence of NbC/TiC particles at the fracture surface (Fig. 15).

The specimens subjected to high-temperature testing are referred to as WC_HT (representing the WM in the centre of the gauge length) and BZ_HT (indicating the buttering zone in the centre of the gauge length). The macrograph of the tensile specimen is displayed in Fig. 16a. The test was performed at 620 °C. Both specimens,

namely WC_HT and BZ_HT, exhibited plastic deformation, as evidenced by necking occurring at the fracture point before the ultimate fracture occurred (Fig. 16b). The stress–strain plot and the variation in tensile properties are illustrated in Fig. 16c, d, respectively. The S_{ut} was determined to be 284 MPa for WC_HT and 290 MPa for BZ_HT, respectively. The fracture location, initially located in the IN82 BZ region during room temperature testing, shifted to the AISI 304L BM region during high-temperature testing (Fig. 16b). The yield strength (S_{yt}) was 165 MP and 155 MPa for WC_HT and BZ_HT, respectively. The % elongation and % reduction in area were found to be the same in both cases. The top view of the fracture surface is depicted in Fig. 16d, and this surface was further analysed using SEM/EDS. Images of this analysis are presented in Fig. 16e, f. The macrograph of the fractured surface (Fig. 16a) reveals evidence of necking prior to fracture, whilst the top view of the fracture surface (Fig. 16d) confirmed its brittleness. The fracture surface exhibited both ductile (dimples and microvoids) and brittle area (Fig. 16e, f) and confirmed the mixed mode dominated fracture. The formation of these profound dimples results from the nucleation, growth and gradual merging

Fig. 16 **a** Macrograph of the tensile specimen tested at high temperature before and after fracture, **b** stress–strain plot, **c** variation in tensile properties, **d** top view of the fractured surface; SEM image of the fracture surface and their EDS, **e** WC_HT, **f** BZ_HT



of vacancies within an atomic lattice subjected to stress, signifying increased ductility in the sample. The average diameter at the fracture tip measured 2.93 mm for WC_HT and 2.77 mm for BZ_HT. The presence of inclusions on the fracture surface is also apparent in Fig. 16e, f. The EDS analysis (E1 and E2) confirms the presence of MnS inclusions. These inclusions serve as localized sites for the initiation of micro-cavities. The inclusions are observed besides the deeper dimples. In the vicinity of the inclusions, the development of cracks in neighbouring planes is expedited, leading to the formation of deeper dimples when compared to other areas. The deeper dimples are seen higher in number for BZ_HT (Fig. 16f). A higher

density of ductile dimples and voids is observed in WC_HT compared to BZ_HT.

4 Conclusions

The paper presents the effect of the IN82 buttering layer on the mechanical and microstructural behaviour of the dissimilar welded joint of grade 92 steel and AISI 304L steel, produced using a multi-pass GTAW process by employing the IN617 filler. The main research findings are mentioned below:

1. The macrograph analysis of the weldments unveiled a noticeable heat-affected zone (HAZ) on the grade 92 steel side, with a width ranging from 1.40 to 4.96 mm. The width of the buttering layer was measured within the range of 5.63 to 6.16 mm.
2. The buttering zone adjacent to the fusion line of grade 92 steel displayed a columnar dendritic microstructure characterized by the presence of both type I and type II boundaries. In this region, grade 92 steel exhibited a higher concentration of the softer δ ferrite. However, when examining the SEM image, a narrow unmixed zone was observed, along with a martensitic layer with a width measuring between 4 and 4.5 μm . A notable area with a filler-deficient zone, characterized by an unmixed zone, islands and peninsulas, was detected near the fusion line on the AISI 304L steel side.
3. The line map analysis across the martensitic layer revealed a notable increase in carbon concentration, confirming the diffusion of carbon. Furthermore, as one moved from the buttering zone towards the fusion line, an increase in Fe concentration and a decrease in Ni and Cr concentration were also confirmed. At the interface between the IN82 BZ and the IN617 weld metal, there was a major concentration gradient for Fe, Ni and Nb, accompanied by the segregation of Ti and Nb-rich phases. The interface between the IN617 weld metal and the AISI 304L BM displayed a distinct concentration gradient for Ni and Fe.
4. Both IN82 BZ and IN617 weld metal exhibited the dendritic microstructure having distinct grain boundaries including SGBs, SSGBs and MGBs. However, the IN82 buttering zone had a greater number of MGBs in comparison to the IN617 weld metal. This difference could be attributed to the higher concentration of alloying elements in the IN617 weld metal, particularly along the inter-dendritic areas. The SEM/EDS study unveiled that the primary concentration of the NbC/TiC phases was observed in the IN82 BZ, whilst the IN617 weld metal showed the presence of Cr and Mo-rich M_{23}C_6 and Mo_6C phases. The density of the carbide phases was also noticed higher in IN617 weld metal than in IN82 BZ.
5. Buttering of grade 92 steel side limited the maximum hardness of the HAZ to 334 HV (in the FGHAZ). The greater density of alloying elements within the inter-dendritic regions and throughout the matrix of the IN617 weld metal resulted in a higher hardness measurement for the IN617 weld metal, which was 276 HV, compared to the IN82 buttering zone, which had a hardness of 221 HV.
6. The ultimate tensile strength (S_{ut}) of WC_RT and BZ_RT was determined to be 607 ± 2 MPa and 592 ± 2 MPa, respectively. These values are close to the minimum required value of 600 MPa. The introduction of the

buttering layer led to a significant increase in ductility ($35 \pm 2\%$) without compromising the S_{ut} . It can be concluded that the joint is safe for application in USC boilers. The S_{ut} for high-temperature tensile tested specimen was found to be 284 MPa for WC_HT and 290 MPa for BZ_HT, respectively with a fracture location in AISI 304L BM.

7. The results of the impact test confirmed the qualification of the weldments for use USC boiler applications. The impact toughness of the WM and BZ were 103 ± 5 J and 72 ± 4 J, respectively.

Author contributions Hardik Sanjay Surkar: Conceptualization; Data curation; Formal analysis; Investigation; Methodology; Roles/Writing -original draft; Writing—review & editing. Amit Kumar: Formal analysis; Investigation; Methodology; Roles/Writing -original draft; Writing—review & editing. Sachin Sirohi: Conceptualization; Data curation; Formal analysis; Investigation; Methodology; Roles/Writing -original draft; Writing—review & editing. Shailesh M Pandey: Conceptualization; Project administration; Resources; Software; Supervision; Validation; Visualisation; Funding acquisition; Investigation; Roles/Writing—original draft. Aleksandra Świerczyńska: Conceptualization; Data curation; Formal analysis; Investigation; Methodology; Roles/Writing -original draft; Writing—review & editing. Dariusz Fydrich: Conceptualization; Project administration; Resources; Software; Supervision; Validation; Visualisation; Funding acquisition; Investigation; Roles/Writing—original draft; Writing—review & editing. Chandan Pandey: Conceptualization; Project administration; Resources; Software; Supervision; Validation; Visualisation; Funding acquisition; Investigation; Roles/Writing—original draft; Writing—review & editing.

Funding No funding is received for the work.

Data and code availability The raw/processed data required to reproduce these findings cannot be shared at this time due to technical or time limitations.

Declarations

Conflict of interest The authors declare that they have no known competing financial interests or personal relationships that could have appeared to influence the work reported in this paper.

Ethical approval Not Applicable.

References

1. Abe F. Research and development of heat-resistant materials for advanced USC power plants with steam temperatures of 700 °C and above. *Engineering*. 2015;1:211–24. <https://doi.org/10.15302/J-ENG-2015031>.
2. Pandey C, Mahapatra MM, Kumar P, Thakre JG, Saini N. Role of evolving microstructure on the mechanical behaviour of P92 steel welded joint in as-welded and post weld heat treated state. *J Mater Process Technol*. 2019;263:241–55. <https://doi.org/10.1016/j.jmatprotec.2018.08.032>.

3. Vaillant JC, Vandenberghe B, Hahn B, Heuser H, Jochum C. T/P23, 24, 911 and 92: new grades for advanced coal-fired power plants-properties and experience. *Int J Press Vessel Pip.* 2008;85:38–46. <https://doi.org/10.1016/j.ijpvp.2007.06.011>.
4. Panneer Selvi S, Prasad Reddy GV. Microstructure and tensile properties of dissimilar weld joint between alloy 800 and buttered Grade 91. *Metall Mater Trans A Phys Metall Mater Sci.* 2023;54:939–51. <https://doi.org/10.1007/s11661-022-06941-6>.
5. Singh P, Arora N, Sharma A. Enhancing mechanical properties and creep performance of 304H and inconel 617 superalloy dissimilar welds for advanced ultra super critical power plants. *Int J Press Vessel Pip.* 2023;201:104882. <https://doi.org/10.1016/j.ijpvp.2022.104882>.
6. Kumar S, Pandey C, Goyal A. A microstructural and mechanical behavior study of heterogeneous P91 welded joint. *Int J Press Vessel Pip.* 2020;185:104128. <https://doi.org/10.1016/j.ijpvp.2020.104128>.
7. Li S, Li J, Sun G, Deng D. Modeling of welding residual stress in a dissimilar metal butt-welded joint between P92 ferritic steel and SUS304 austenitic stainless steel. *J Mater Res Technol.* 2023;23:4938–54. <https://doi.org/10.1016/j.jmrt.2023.02.123>.
8. Taraphdar PK, Kumar R, Pandey C, Mahapatra MM. Significance of finite element models and solid-state phase transformation on the evaluation of weld induced residual stresses. *Met Mater Int.* 2021;27:3478–92. <https://doi.org/10.1007/s12540-020-00921-4>.
9. Kulkarni A, Dwivedi DK, Vasudevan M. Dissimilar metal welding of P91 steel-AISI 316L SS with Incoloy 800 and Inconel 600 interlayers by using activated TIG welding process and its effect on the microstructure and mechanical properties. *J Mater Process Technol.* 2019;274:116280. <https://doi.org/10.1016/j.jmatprotec.2019.116280>.
10. Cao J, Gong Y, Yang ZG, Luo XM, Gu FM, Hu ZF. Creep fracture behavior of dissimilar weld joints between T92 martensitic and HR3C austenitic steels. *Int J Press Vessel Pip.* 2011;88:94–8. <https://doi.org/10.1016/j.ijpvp.2011.01.003>.
11. Pavan AHV, Ravibharath R, Singh K. Creep-rupture behavior of SUS 304H – IN 617 dissimilar metal welds for AISC boiler applications. *Mater Sci Forum.* 2015;830–831:199–202. <https://doi.org/10.4028/www.scientific.net/MSF.830-831.199>.
12. Chitturi V, Pedapati SR, Awang M. Mathematical model for friction stir lap welded AA5052 and SS304 joints and process parameters optimization for high joint strength. *Adv Mater Sci.* 2022;22:5–22. <https://doi.org/10.2478/adms-2022-0001>.
13. Shah Hosseini H, Shamanian M, Kermanpur A. Characterization of microstructures and mechanical properties of Inconel 617/310 stainless steel dissimilar welds. *Mater Charact.* 2011;62:425–31. <https://doi.org/10.1016/j.matchar.2011.02.003>.
14. Shah Hosseini H, Shamanian M, Kermanpur A. Microstructural and weldability analysis of Inconel617/AISI 310 stainless steel dissimilar welds. *Int J Press Vessel Pip.* 2016;144:18–24. <https://doi.org/10.1016/j.ijpvp.2016.05.004>.
15. Cao J, Gong Y, Zhu K, Yang ZG, Luo XM, Gu FM. Microstructure and mechanical properties of dissimilar materials joints between T92 martensitic and S304H austenitic steels. *Mater Des.* 2011;32:2763–70. <https://doi.org/10.1016/j.matdes.2011.01.008>.
16. Cao J, Gong Y, Yang Z. Microstructural analysis on creep properties of dissimilar materials joints between T92 martensitic and HR3C austenitic steels. *Mater Sci Eng A.* 2011;528:6103–11. <https://doi.org/10.1016/j.msea.2011.04.057>.
17. Kim MY, Kwak SC, Choi IS, Lee YK, Suh JY, Fleury E, Jung WS, Son TH. High-temperature tensile and creep deformation of cross-weld specimens of weld joint between T92 martensitic and Super304H austenitic steels. *Mater Charact.* 2014;97:161–8. <https://doi.org/10.1016/j.matchar.2014.09.011>.
18. Kumar A, Pandey SM, Bhattacharya A, Fydrych D, Sirohi S, Pandey C. Selection of electrode material for inconel 617/P92 Steel SMAW dissimilar welds. *J Press Vessel Technol.* 2023;145:1–11. <https://doi.org/10.1115/1.4062794>.
19. Naffakh H, Shamanian M, Ashrafzadeh F. Dissimilar welding of AISI 310 austenitic stainless steel to nickel-based alloy Inconel 657. *J Mater Process Technol.* 2009;209:3628–39. <https://doi.org/10.1016/j.jmatprotec.2008.08.019>.
20. J.M. Race. Carbon Diffusion Across Dissimilar Steel Welds, PhD Thesis. (1992).
21. Zhao Y, Gong J, Wang X, Gao W, Li Q. Carbon diffusion in dissimilar joints between P91 and 12Cr1MoV steels welded by different consumables at high temperature. *Mater High Temp.* 2015;32:557–65. <https://doi.org/10.1179/1878641315Y.000000002>.
22. Sudha C, Paul VT, Terrance ALE, Saroja S, Vijayalakshmi M. Microstructure and microchemistry of hard zone in dissimilar weldments of Cr-Mo steels. *Weld. J. (Miami, Fla.)*. 85 (2006).
23. Guo X, He P, Xu K, Lv XC, Zhang JB, Gu Y. Microstructure investigation on the fusion zone of steel/nickel-alloy dissimilar weld joint for nozzle buttering in nuclear power industry. *Weld World.* 2021. <https://doi.org/10.1007/s40194-021-01199-9>.
24. Shariatpanahi AM, Farhangi H. Microstructure and mechanical properties of dissimilar ferritic and austenitic steel joints with an intermediate Inconel-182 buttering layer. *Adv Mater Res.* 2010;83–86:449–56. <https://doi.org/10.4028/www.scientific.net/AMR.83-86.449>.
25. Hytönen N, Ge Y, Que Z, Lindqvist S, Nevasmaa P, Virkkunen I, Efsing P. Study of fusion boundary microstructure and local mismatch of SA508/ally 52 dissimilar metal weld with buttering. *J Nucl Mater.* 2023. <https://doi.org/10.1016/j.jnucmat.2023.154558>.
26. Bhaduri AK, Venkadesan S, Rodriguez P, Mukunda PG. Transition metal joints for steam generators—an overview. *Int J Press Vessel Pip.* 1994;58:251–65. [https://doi.org/10.1016/0308-0161\(94\)90061-2](https://doi.org/10.1016/0308-0161(94)90061-2).
27. Pavan AHV, Vikrant KSN, Ravibharath R, Singh K. Development and evaluation of SUS 304H—IN 617 welds for advanced ultra supercritical boiler applications. *Mater Sci Eng A.* 2015;642:32–41. <https://doi.org/10.1016/j.msea.2015.06.065>.
28. Dak G, Pandey SM, Pandey C. Residual stress analysis, microstructural characterization, and mechanical properties of tungsten inert gas-welded P92/AISI 304L dissimilar steel joints. *Proc Inst Mech Eng Part L J Mater Des Appl.* 2023;237:767–90. <https://doi.org/10.1177/14644207221124494>.
29. Kumar A, Pandey C. Autogenous laser-welded dissimilar joint of ferritic/martensitic P92 steel and Inconel 617 alloy: mechanism, microstructure, and mechanical properties. *Arch Civ Mech Eng.* 2022;22:39. <https://doi.org/10.1007/s43452-021-00365-6>.
30. Rathod DW, Pandey S, Aravindan S, Singh PK. Metallurgical behaviour and carbon diffusion in buttering deposits prepared with and without buffer layers. *Acta Metall Sin (English) Lett.* 2017;30:120–32. <https://doi.org/10.1007/s40195-016-0487-x>.
31. Rathod DW, Pandey S, Aravindan S, Singh PK. Diffusion control and metallurgical behavior of successive buttering on SA508 steel using Ni–Fe alloy and inconel 182. *Metallogr Microstruc Anal.* 2016;5:450–60. <https://doi.org/10.1007/s13632-016-0311-z>.
32. Saffari H, Shamanian M, Bahrami A, Szpunar JA. Effects of ERNiCr-3 butter layer on the microstructure and mechanical properties of API 5L X65/AISI304 dissimilar joint. *J Manuf Process.* 2020;50:305–18. <https://doi.org/10.1016/j.jmapro.2019.12.028>.
33. Ahmad HW, Chaudry UM, Tariq MR, Shoukat AA, Bae DH. Assessment of fatigue and electrochemical corrosion characteristics of dissimilar materials weld between alloy 617 and 12 Cr steel. *J Manuf Process.* 2020;53:275–82. <https://doi.org/10.1016/j.jmapro.2020.02.038>.

34. Dak G, Singh V, Kumar A, Sirohi S, Bhattacharyya A, Pandey C, Pandey SM. Microstructure and mechanical behaviour study of the dissimilar weldment of 'IN82 buttered' P92 steel and AISI 304L steel for ultra super critical power plants. *Mater Today Commun.* 2023;37:107552. <https://doi.org/10.1016/j.mtcomm.2023.107552>.
35. DuPont JN, Lippold JC, Kiser SD. *Welding metallurgy and weldability of nickel-base alloys.* Wiley. 2009. <https://doi.org/10.1002/9780470500262>.
36. Dak G, Khanna N, Pandey C. Study on narrow gap welding of martensitic grade P92 and austenitic grade AISI 304L SS steel for ultra-supercritical power plant application. *Arch Civ Mech Eng.* 2023;23:14. <https://doi.org/10.1007/s43452-022-00540-3>.
37. Kumar A, Pandey C. Development and evaluation of dissimilar gas tungsten arc-welded joint of P92 steel/inconel 617 alloy for advanced ultra-supercritical boiler applications. *Metall Mater Trans A.* 2022;53:3245–73. <https://doi.org/10.1007/s11661-022-06723-0>.
38. Elongation P, ERNiCrCoMo-1 DATA SHEET, 1 (n.d.) 0–1.
39. ASTM E8. ASTM E8/E8M standard test methods for tension testing of metallic materials I. *Annu B ASTM Stand.* 2010;4:1–27. <https://doi.org/10.1520/E0008>.
40. Akram J, Kalvala PR, Chalavadi P, Misra M. Dissimilar metal weld joints of P91/Ni alloy: microstructural characterization of HAZ of P91 and stress analysis at the weld interfaces. *J Mater Eng Perform.* 2018;27:4115–28. <https://doi.org/10.1007/s11665-018-3502-8>.
41. A. E23-02a, ASTM E23-02a - Notched Bar Impact Testing of Metallic Materials . pdf, ASTM Int. (2002).
42. Dak G, Pandey C. Microstructure anomaly during welding and its influence on the mechanical properties of dissimilar weldments of P92 martensitic steel and AISI 304L austenitic stainless steel. *J Manuf Process.* 2022;80:829–51.
43. Rojas D, Garcia J, Prat O, Sauthoff G, Kaysser-Pyzalla AR. 9%Cr heat resistant steels: alloy design, microstructure evolution and creep response at 650°C. *Mater Sci Eng A.* 2011;528:5164–76. <https://doi.org/10.1016/j.msea.2011.03.037>.
44. Laha K, Chandravathi KS, Parameswaran P, Goyal S, Mathew MD. A comparison of creep rupture strength of ferritic/austenitic dissimilar weld joints of different grades of Cr-Mo ferritic steels. *Metall Mater Trans A.* 2012;43:1174–86. <https://doi.org/10.1007/s11661-011-0957-8>.
45. Hou J, Peng Q, Takeda Y, Kuniya J, Shoji T. Microstructure and stress corrosion cracking of the fusion boundary region in an alloy 182–A533B low alloy steel dissimilar weld joint. *Corros Sci.* 2010;52:3949–54. <https://doi.org/10.1016/j.corsci.2010.08.002>.
46. Ming H, Zhu R, Zhang Z, Wang J, Han EH, Ke W, Su M. Microstructure, local mechanical properties and stress corrosion cracking susceptibility of an SA508-52M-316LN safe-end dissimilar metal weld joint by GTAW. *Mater Sci Eng A.* 2016;669:279–90. <https://doi.org/10.1016/j.msea.2016.05.101>.
47. Mougnot R, Hänninen H. Microstructures of nickel- base alloy dissimilar metal welds, n.d.
48. Soysal T, Kou S, Tat D, Pasang T. Macrosegregation in dissimilar-metal fusion welding. *Acta Mater.* 2016;110:149–60. <https://doi.org/10.1016/j.actamat.2016.03.004>.
49. Kumar S, Pandey C, Goyal A. Microstructure and mechanical behavior of P91 steel dissimilar welded joints made with IN718 filler. *Int J Press Vessel Pip.* 2021;190:104290. <https://doi.org/10.1016/j.ijpvp.2020.104290>.
50. Dupont JN, Kusko CS. Technical note: martensite formation in austenitic/ferritic dissimilar alloy welds. *Weld J.* 2007;86:51s.
51. Zhang Y, Jing H, Xu L, Han Y, Zhao L, Xiao B. Microstructure and mechanical performance of welded joint between a novel heat-resistant steel and Inconel 617 weld metal. *Mater Charact.* 2018;139:279–92. <https://doi.org/10.1016/j.matchar.2018.03.012>.
52. Sirohi S, Taraphdar PK, Dak G, Pandey C, Sharma SK, Goyal A. Study on evaluation of through-thickness residual stresses and microstructure-mechanical property relation for dissimilar welded joint of modified 9Cr–1Mo and SS304H steel. *Int J Press Vessel Pip.* 2021;194:104557. <https://doi.org/10.1016/j.ijpvp.2021.104557>.
53. Kulkarni A, Dwivedi DK, Vasudevan M. Study of mechanism, microstructure and mechanical properties of activated flux TIG welded P91 Steel-P22 steel dissimilar metal joint. *Mater Sci Eng A.* 2018;731:309–23. <https://doi.org/10.1016/j.msea.2018.06.054>.

Publisher's Note Springer Nature remains neutral with regard to jurisdictional claims in published maps and institutional affiliations.

Springer Nature or its licensor (e.g. a society or other partner) holds exclusive rights to this article under a publishing agreement with the author(s) or other rightsholder(s); author self-archiving of the accepted manuscript version of this article is solely governed by the terms of such publishing agreement and applicable law.